

# Observations of gravity waves in the OH airglow layer above Rothera (68S, 68W) using a three-dimensional S-Transform analysis

Shaun Martin Dempsey<sup>1</sup>, Neil P Hindley<sup>1</sup>, Corwin James Wright<sup>1</sup>, Nicholas Mitchell<sup>1</sup>, Tracy Moffat-Griffin<sup>2</sup>, Pierre-Dominique Pautet<sup>3</sup>, and Michael J. Taylor<sup>4</sup>

<sup>1</sup>University of Bath

<sup>2</sup>British Antarctic Survey

<sup>3</sup>Utah State University

<sup>4</sup>Utah State University

January 17, 2023

## Abstract

In this study, we apply the three-dimensional Stockwell Transform (3DST) to a novel dataset, namely airglow imager data from Rothera (68S, 68W). We use this approach to investigate small-scale high-frequency gravity waves (GWs) in the hydroxyl (OH) airglow layer, at a height  $\sim 87$  km in the mesosphere and lower thermosphere (MLT). MLT GWs are often underrepresented in models, being parameterised due to their small scale size and as such, the significant quantities of momentum and energy transferred by these small waves are missed. Better quantification of these waves is thus needed to support future model development. We find that the 3DST can identify waves and extract wave properties and their locations. Horizontal wavelengths are observed ranging from 10 to 40 km and vertical wavelengths of 15 to 40 km, with wave periods of 5 to 9 minutes, peaking at 7.5 minutes. These values are consistent with previous studies. Group speeds are found to be non-zero and large, implying that these GWs travel horizontally and fast. This case study demonstrates that the 3DST can be applied to airglow imager data and can successfully extract GW parameters. This is an important step in automating GW analysis in airglow.



**Abstract**

In this study, we apply the three-dimensional Stockwell Transform (3DST) to a novel dataset, namely airglow imager data from Rothera (68°S, 68°W). We use this approach to investigate small-scale high-frequency gravity waves (GWs) in the hydroxyl (OH) airglow layer, at a height  $\sim 87$  km in the mesosphere and lower thermosphere (MLT). MLT GWs are often underrepresented in models, being parameterised due to their small scale size and as such, the significant quantities of momentum and energy transferred by these small waves are missed. Better quantification of these waves is thus required to support future model development. We find that the 3DST can identify waves and extract wave properties and their locations. Horizontal wavelengths are observed ranging from 10 to 40 km and vertical wavelengths of 15 to 40 km, with wave periods of 5 to 9 minutes, peaking at 7.5 minutes. These values are consistent with previous studies. Group speeds are found to be non-zero and large, implying that these GWs travel horizontally and fast. This case study demonstrates that the 3DST can be applied to airglow imager data and can successfully extract GW parameters. This is an important step in automating GW analysis in airglow.

**1 Introduction**

Atmospheric gravity waves (GWs) are fluid-dynamical waves which propagate through the atmosphere and are critical to the dynamics, transport and circulation of the stratosphere, mesosphere and thermosphere (Fritts & Alexander, 2003; Fritts et al., 2006). They are mainly generated in the lower atmosphere by sources including mountains, convective storms, and dynamical systems such as jets, and have spatial scales of ten to hundreds of kilometres and temporal scales from five minutes to several hours.

Due to the decrease of density with height, GWs grow in amplitude as they ascend into the mesosphere and lower thermosphere, eventually overturning, breaking and depositing the energy and momentum they transport from their source into the mean flow. This deposition is sufficiently large to force a meridional flow through zonal drag, driving the mesopause temperature up to 100 K from radiative equilibrium ((Lindzen, 1981; Becker, 2012), and initiating a residual circulation from the cold summer to the warm winter pole. As global circulation models extend upwards into the mesosphere/lower thermosphere (MLT) system and beyond, they must hence be able to reproduce either GWs and/or the energy and momentum they transport accurately. Current models fail to recreate much of the GW activity responsible for controlling and determining the global circulation, as the waves exist at spatial and temporal scales which are not resolved by models of this type. To compensate for this missing effect, the waves are instead parameterised in such models. To do so effectively, the GW parametrisations must be tuned to represent the real atmosphere, accurately depicting the waves' impact on the atmosphere.

Previous observational and modelling studies have found that GW activity is particularly intense in the wintertime over the Southern Andes and the Antarctic Peninsula (Kogure et al., 2021; Hindley et al., 2015; Baumgaertner & McDonald, 2007; Alexander & Teitelbaum, 2007). This region is distinguished by steep topography, high winds over the Southern Ocean, and ferocious frontal activity, which together lead to the generation of strong orographic, convective, and jet-front GWs. As such, knowledge of the behaviour of the waves in the MLT above this region is especially important to guide future model development. This strong GW activity is well-known, and as such a wide range of wave-resolving instruments have been deployed to this region over the past few decades. Consequently, we are now able to investigate these GWs in many ways, such as satellites, rockets, balloons and ground-based techniques (Hindley et al., 2022; Perrett et al., 2021; Hindley et al., 2019; Moffat-Griffin & Colwell, 2017; Wright et al., 2017; Wüst & Bittner, 2008; Goldberg, 2004; Yoshimura et al., 2003).

68 One commonly-used technique for both satellite and ground-based GWs observa-  
 69 tions is to exploit atmospheric airglow. Physically, this airglow is caused by photon emis-  
 70 sions from chemiluminescent processes which involve species such as atomic oxygen, atomic  
 71 nitrogen, and hydroxyl radicals (Khomich et al., 2008). This phenomenon, also known  
 72 as nightglow, acts as a passive tracer for atmospheric dynamics in the MLT, facilitat-  
 73 ing the study of GWs via imagers, rockets and satellites (e.g. Ganaie et al. (2022); Kogure  
 74 et al. (2020); Hu, Ma, Yan, Hindley, Xu, and Jiang (2019a); Miller et al. (2015); Gard-  
 75 ner and Taylor (1998); Takahashi et al. (1996); Taylor et al. (1993); Peterson (1979)).

76 Several energy bands contribute to the total visible and short-wave infrared air-  
 77 glow intensity observed at ground level, but the intensity in the short-wave infrared re-  
 78 gion is substantially higher in hydroxyl (OH) than at other infrared wavelengths. Specif-  
 79 ically, in the short-wave infrared regime lie the Meinel bands, initially studied by Meinel  
 80 (1950), which arise from rotational and vibrational atomic transitions (von Savigny, 2015).  
 81 OH is the primary radiation source of the near-infrared (NIR) airglow layer, which is cen-  
 82 tred at 87 km in height and has a full-width-half-maximum of around 8 km (Baker &  
 83 Stair, 1988), varying in altitude by typically a few kilometres (von Savigny, 2015; Wüst  
 84 et al., 2016, 2022).

85 GWs appear in airglow layers as a result of changes in pressure and temperature  
 86 caused by the waves passing through the medium, which lead to intensity fluctuations  
 87 in the observed emitted radiation. Many previous studies have shown that OH airglow  
 88 emissions are excellent tracers for observing atmospheric properties and studying dynam-  
 89 ical processes such as instabilities, ripples, small-scale GWs, and larger-scale atmospheric  
 90 waves such as tides and planetary waves (Sedlak et al., 2020; J. Li et al., 2017; Cao &  
 91 Liu, 2016). The spectral properties of small-scale GWs in the MLT, such as wavelengths,  
 92 phase speeds, and propagation directions, can hence be directly observed in the airglow  
 93 layers by using optical imagers. Previous studies have observed GWs with typical hor-  
 94 izontal wavelengths of 20-100 km, intrinsic wave periods of 5 – 10 minutes, and horizon-  
 95 tal phase speeds ranging from 30 to 100  $\text{ms}^{-1}$  (Ejiri et al., 2003; Taylor et al., 1997; Z. Li  
 96 et al., 2011). These limits are imposed by the spatial extent airglow imagers can observe  
 97 and the cadence of images taken.

98 In this study, we present a novel application of the three-dimensional Stockwell Trans-  
 99 form (S-Transform) to OH airglow imager data from the British Antarctic Survey base  
 100 at Rothera (68°S, 68°W), using data from the night of the 26th – 27th April 2012 as both  
 101 as a case study and a demonstration of the technique. We use the S-Transform to ob-  
 102 serve wave parameters (i.e. wavelengths and periods) and then calculate meteor radar  
 103 winds from the same location to compensate for the Doppler-shifting effects of the wind  
 104 and establish ‘intrinsic’ wave parameters, i.e. in the frame of reference of the wave.

105 In Section 2 we describe the data sources, firstly from the airglow imager and sec-  
 106 ondly from the meteor radar. Section 3 deals, firstly, with the airglow image processing,  
 107 secondly with the S-Transform analysis, thirdly with the meteor radar winds and finally  
 108 with the calculation of wave parameters. Section 5 discusses our method and results in  
 109 the context of previous studies. Finally, in Section 6 we provide our conclusions and a  
 110 future outlook on how this semi-automated method could be applied more broadly.

## 111 2 Data

### 112 2.1 Airglow Imager

113 Airglow imagers have an extensive track record as a tool for detecting and char-  
 114 acterising GWs in atmospheric airglow layers (e.g. Nielsen et al. (2009); Matsuda et al.  
 115 (2014); Rourke et al. (2017)). Here, we use an all-sky (180°) monochromatic filter imag-  
 116 ing system to observe GWs in the  $\sim 87$  km OH airglow layer. The specific instrument used  
 117 measures these OH signals with a 15-second exposure period, and also measures weaker

118 O<sub>2</sub> and Na signals at 90-second and 120-second exposure periods respectively. Combined,  
 119 this gives an overall measurement cadence of  $\sim 6$  min with an embedded 2-minute OH  
 120 cadence. Figure 1 illustrates the approximate emission distribution of these layers as a  
 121 function of height; we use only the OH data here as proof-of-concept, but future stud-  
 122 ies could exploit these additional layers to provide 4D (i.e. distance/height/time) GW  
 123 information from the same site. Similar systems have been used in past studies to anal-  
 124 yse short-period GWs (e.g. Taylor et al. (1997); Pautet (2005); Nielsen et al. (2006))

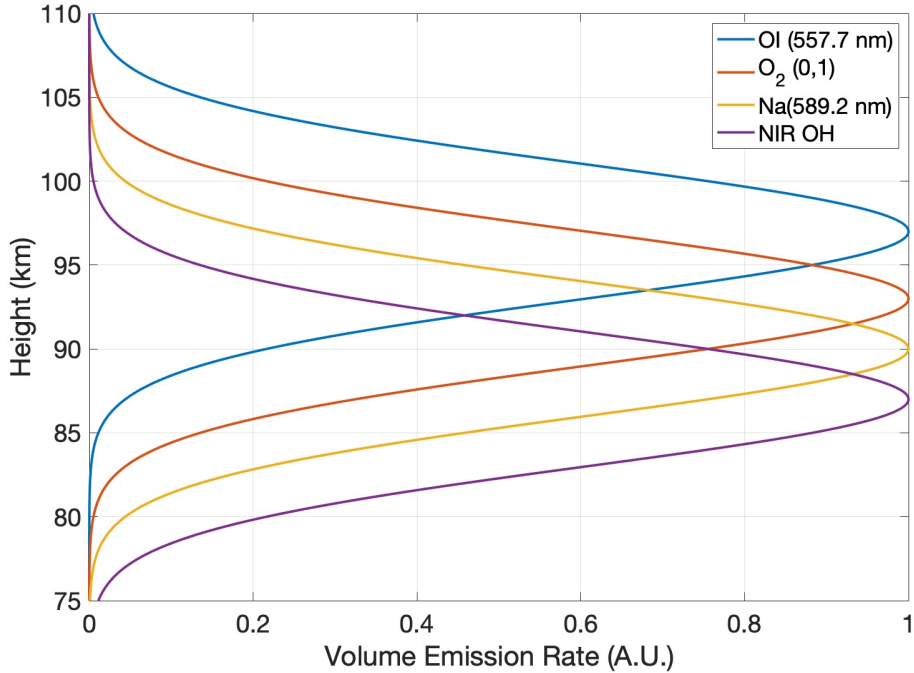


**Figure 1.** Diagrammatic representation of the heights and volume emission rate of four MLT airglow species. Adapted from Nielsen (2007).

## 125 2.2 Meteor Radar

126 Meteor radars are a well-established means of monitoring MLT winds at heights  
 127 from 75 to 105 km. As such, they have been widely used for ground-based tidal and GW  
 128 studies (e.g. Hindley et al. (2022); Stober et al. (2021); Dempsey et al. (2021); Davis et  
 129 al. (2013); Beldon et al. (2006); Mitchell (2002)).

130 Here, we use a SKYiMET meteor radar located at the British Antarctic Survey base  
 131 at Rothera (68°S, 68°W).

132 This instrument was deployed in 2005 and has been operating almost continuously  
 133 from 2005 up to the present. Hocking et al. (2001) provide a full explanation of the SKiYMET  
 134 radar operation.

135 We calculate horizontal winds from raw meteor measurements according to the method  
 136 outlined by Hindley et al. (2022), combining the inferred individual horizontal veloci-  
 137 ties for each meteor using a Gaussian weighting in height and time around a specified  
 138 height and time. These Gaussian weightings have full-width-half-maxima of 2 hours in  
 139 time and 3 km in height. We move the centre of each Gaussian over the data in 1 hour

140 time and 1 km height steps, yielding winds at an hourly resolution across the height range  
 141 from 75 to 105 km. This approach has previously been applied by both Dempsey et al.  
 142 (2021) and Hindley et al. (2022). We use these inferred winds to convert our GW mea-  
 143 surements from the ground-based to the intrinsic frame of reference, linearly interpolat-  
 144 ing the winds to the time of each airglow image to provide local zonal and meridional  
 145 wind estimates.

### 146 3 Method

147 Our S-Transform GW analysis, described below, is based on a Fourier Transform  
 148 algorithm and thus requires the input data to be regularly-gridded in both space and time.  
 149 We also need to remove fast- and slowly-varying background features. Accordingly, the  
 150 data require some preprocessing before they can be analysed. Figure 2 presents the steps  
 151 in our airglow image preprocessing and processing chain. The units of the data are ar-  
 152 bitrary brightness units recorded by the imager, but are consistent between panels.

153 Figure 2a shows an example raw image obtained from the instrument. GWs are  
 154 visually apparent in the frame as curved striped features, but are overlaid by consider-  
 155 able noise from stars and from the Milky Way Galaxy, which in this frame runs through  
 156 the middle of the image. In addition, as there is no geographic metadata stored by the  
 157 imager other than the time of each frame, we need to produce this geographic informa-  
 158 tion.

159 Therefore, we must first convert the observed pixel positions to a spatial location  
 160 (i.e. latitude and longitude) and also remove the stars and the galaxy. The galaxy re-  
 161 moval step is particularly important in this regard: as it is a bright rotating near-linear  
 162 object, application of spectral analysis techniques are likely to identify its rotation as the  
 163 wave to be studied, rather than the overlying small amplitude ripples and bands which  
 164 are the our target.

#### 165 3.1 Airglow Imager Geometry

166 We first convert coordinate frames, with the aim of geolocation each pixel in the  
 167 raw data to a specific spatial distance and direction from the centre of rotation of the  
 168 image, i.e. the vertical axis above the imager. For this purpose, we assume (i) that the  
 169 airglow layer we are observing is at 87 km, (ii) that the zenith, i.e. directly above the Rothera  
 170 airglow imager, is in the middle of the frame and (iii) that the edge of the frame repre-  
 171 sents the horizontal plane of the ground. Using the angle subtended by each pixel from  
 172 the centre pixel, we can then geometrically calculate the latitude and longitude, or ra-  
 173 dius and direction, of each point in the frame.

174 Figure 3 presents the geometry of the airglow layer used to compute this conver-  
 175 sion. To do this, we calculate the arc length,  $a$ , from the zenith position. Under the as-  
 176 sumption that the airglow layer is at a height  $h$  of 87 km above the observer at  $P$ , each  
 177 pixel location  $Q$  makes a right-angled triangle with angle  $\theta$  subtended. This angle allows  
 178 us to calculate the arc length,  $a$ , of the point  $Q$ .  $R_E$  is the radius of the Earth and  $r =$   
 179  $R_E + h$ .

180 The first step is to calculate the location of  $P$  in the PQ plane,  $P^+$ . This is given  
 181 by:

$$P^+ = (P_x^+, P_y^+) = (R_E \cos \theta, R_E \sin \theta) \quad (1)$$

182 We may use this to calculate the angle  $\beta$  as:

$$\beta = \phi - \alpha \quad (2)$$

## Airglow Imager Data Processing

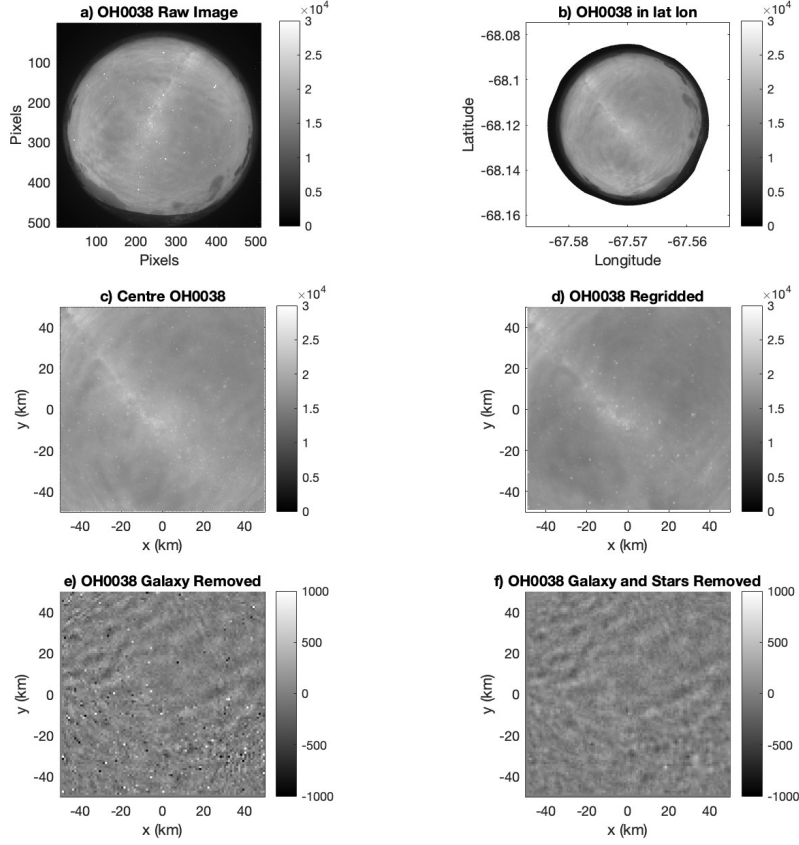


**Figure 2.** Processing steps of the airglow images explained for one image. Panel a) presents the raw image as given in the tif file, b) presents the image projected on a latitude/longitude grid, c) is the centre 100 km square around the zenith, d) is the centre 100 km around the zenith interpolated onto a regularly spaced grid, e) is the centre grid following the FFT galaxy removal and finally f) presents the field of view with a final step of star removal performed.

$$\tan\alpha = \frac{P_x^+}{P_y^+} \quad (3)$$

$$\cos\phi = \frac{P_y^+}{r} \quad (4)$$

183

This means that:

$$\beta = \cos^{-1}\left(\frac{P_y^+}{r}\right) - \tan^{-1}\left(\frac{P_x^+}{P_y^+}\right) \quad (5)$$

$$\beta = \cos^{-1}\left(\frac{R_E \sin\theta}{r}\right) - \tan^{-1}\left(\frac{R_E \cos\theta}{R_E \sin\theta}\right) \quad (6)$$

184

The arc length is therefore given by:



203 pixels. Only pixels exceeding a cutoff of the 98th percentile are dealt with this way, and  
 204 this does leave some stellar signatures which we address below. We can see that we have  
 205 not lost any geophysical information concerning the airglow layer in this step, and the  
 206 waves present in the original image can still be seen.

207 We now move onto the dominant background feature of the Milky Way galaxy. This  
 208 is one of the most visually noticeable features of the sky, especially in dark locations such  
 209 as Rothera. To remove this signal do this, we perform a three-dimensional FFT on the  
 210 image and then remove low temporal frequencies, i.e. signals with long and regular tem-  
 211 poral periods. This is done using a 3D Fast Fourier Transform, the inverse FFT returns  
 212 Figure 2e, in which the signature of the galaxy has been very significantly ameliorated.  
 213 The stars, however, are still present in the frame and could be identified by the S-Transform  
 214 as strong waves with very short periods and wavelengths. The final step, therefore, is  
 215 to more strongly remove the stars. We do this using a difference filter, where we com-  
 216 pute the difference between adjacent pixels time, i.e. between frames. Specifically, we  
 217 identify those pixels which show a difference of over 300 (in arbitrary units) between frames  
 218 and remove the value, replacing it with the mean of the surrounding values. This returns  
 219 Figure 2f where the processed data appears with no strong signatures of either stars or  
 220 the galaxy and with the target waves now very visually prominent.

### 221 3.2 S-transform Wave Analysis

222 When extracting wave properties from airglow data, a conventional Fourier trans-  
 223 form analysis can identify the frequencies present in the data; however, it cannot iden-  
 224 tify where and when these frequencies occur in geospatial coordinates. For this, another  
 225 method is required. Accordingly, in this study we apply the 3-D Stockwell transform (3DST)  
 226 technique described by Wright et al. (2017) and Hindley et al. (2019) to measure the spec-  
 227 tral properties of GWs, using two dimensions of space (northwards and eastwards) and  
 228 one of time. Based upon the work of R. Stockwell et al. (1996) and Hindley et al. (2016),  
 229 this method provides a voxel-by-voxel estimate of the amplitude, spatial and temporal  
 230 frequency and direction of propagation of the strongest wavelike signal at every location  
 231 in the 3-D (i.e.  $x, y, t$ ) data volume. From these estimated properties, we are further able  
 232 to infer properties such as phase speed and vertical wavelength, as described below.

233 The S-transform has been extensively used in previous GW studies (R. G. Stock-  
 234 well & Lowe, 2001; McDonald, 2012; Wright & Gille, 2013; Hindley et al., 2016; Hu, Ma,  
 235 Yan, Hindley, Xu, & Jiang, 2019b; Hu, Ma, Yan, Hindley, & Zhao, 2019; Hindley et al.,  
 236 2019), and demonstrated to be a highly capable technique for measuring and localising  
 237 frequencies (or wavenumbers) and their associated amplitudes. However, these previous  
 238 gravity wave studies have used it in spatial dimensions only, and applying it to mixed  
 239 space/time data as we do here is a novel approach. By limiting the range of permitted  
 240 frequencies over which the spectral windows are applied, we are also in principle able to  
 241 select for different periods and wavelengths to allow the investigation of ripples and bands;  
 242 however, as this study is a demonstration of the method, we have not, in this case, re-  
 243 stricted the frequencies detected in this way.

### 244 3.3 Calculating Wave Properties

245 With the measured parameters from the S-Transform, supported by wind data from  
 246 the meteor radar, we can calculate both observed and intrinsic wave parameters, i.e. the  
 247 wave parameters in both ground-based Eulerian and wind-following Lagrangian frames  
 248 of reference.

249 To do this, we first use the 3DST to measure the horizontal wavenumbers ( $k$  and  
 250  $l$  in the zonal and meridional directions, respectively), period, frequencies, wavelengths  
 251 and amplitudes of the observed waves. From these, we can directly compute the hori-

252 zontal wave phase speed  $c_p$  as  $c_p = \omega/k_h$ , where  $\omega$  is the measured angular frequency  
 253 and  $k_h$  is the Pythagorean sum of  $k$  and  $l$ . We can then calculate the intrinsic frequency,  
 254  $\hat{\omega}$ , given by

$$\hat{\omega} = \omega - k\bar{u} - l\bar{v} \quad (9)$$

255 where  $\bar{u}$  is the background zonal wind and  $\bar{v}$  is the background meridional wind. To do  
 256 this, we use hourly wind values from the radar data linearly interpolated to each image  
 257 time.

258 The intrinsic horizontal phase speed,  $\hat{c}_p$ , can then be computed as  $\hat{c}_p = c_p - \bar{u}_h$   
 259 where  $\bar{u}_h$  is the Pythagorean sum of  $u$  and  $v$ . Using the medium frequency GW approx-  
 260 imation (Fritts & Alexander, 2003), such that the absolute value of vertical wavenum-  
 261 ber,  $m$ , is given by  $|m| = N/|\hat{c}_p|$  where  $N$  is the Brunt-Väisälä frequency and  $\hat{c}_h$  is the  
 262 intrinsic horizontal phase speed, this allows us to calculate  $\lambda_z = 1/m$ .

263 We can then calculate the intrinsic frequency:

$$\hat{\omega} = N \left| \frac{k_h}{m} \right| \quad (10)$$

264 and also the intrinsic group speed  $\hat{c}_g$ :

$$\hat{c}_g = \bar{u} + \frac{\hat{\omega}}{k_h} \quad (11)$$

265 Once we have performed these calculations we have the following parameters:

- 266 • horizontal and vertical wavelengths,  $\lambda_h$  and  $\lambda_z$ , respectively
- 267 • observed and intrinsic frequencies,  $\omega$  and  $\hat{\omega}$ , respectively
- 268 • observed and intrinsic horizontal phase speeds,  $c_p$  and  $\hat{c}_p$ , respectively
- 269 • observed and intrinsic group speeds,  $c_g$  and  $\hat{c}_g$ , respectively
- 270 • direction
- 271 • and finally period  $T$ .

## 272 4 Results

### 273 4.1 Initial Visual Analysis

274 Figure 4 presents a time series of waves above an S-Transform-derived amplitude  
 275 threshold over the time period 23:35 to 01:05 on the night of the 26th – 27th of April  
 276 2012.

277 In this figure, to highlight only the strongest wave features results are only shown  
 278 where the S-Transform output amplitude is above a cutoff value of 200 units, illustrated  
 279 by a faint semitransparent grey wrapper. This cutoff represents a value close to the 90th  
 280 percentile of the full measured amplitude distribution including noise-dominated regions.  
 281 Within this volume, red and blue isosurfaces represent phase fronts of positive and neg-  
 282 ative perturbations from the background state as the wave moves across the imager’s field  
 283 of view; the outer (semi-transparent) red and blue surfaces enclose values greater than  
 284 10 units and the solid inner surfaces values greater than 45 units.

285 The blue and red isosurfaces can then be interpreted as a visual depiction of the  
 286 wave’s phase fronts as they advance through time. Distinct wavefronts can be seen through-  
 287 out the chosen period, with the region falling within the amplitude cutoff envelope grad-  
 288 ually increasing as the wave covers a larger fraction of the total observed area. We also

289 see two instances of other waves growing and then dissipating separately to the main wave  
 290 envelope. We thus conclude that these waves are indeed persistent and large enough to  
 291 proceed with our investigation.

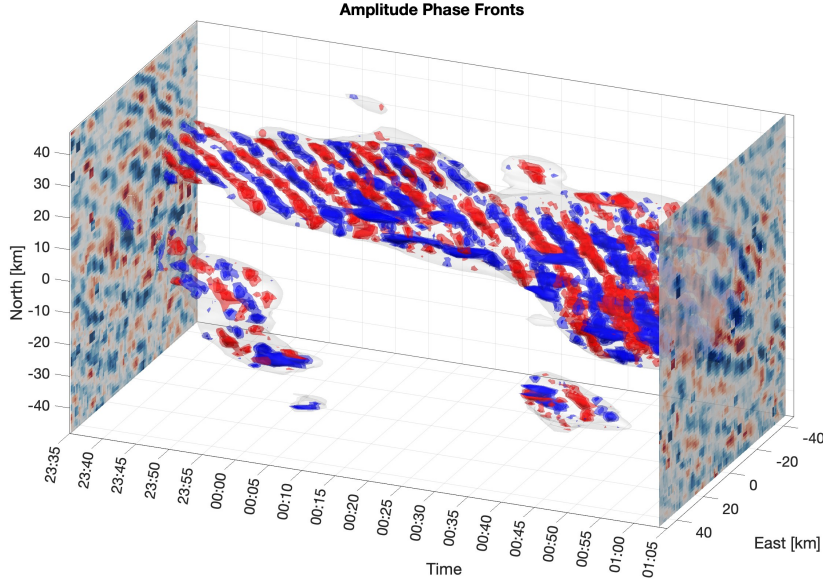


**Figure 4.** 3D visualisation of wave phase fronts over the time period 23:25 to 01:05 on the night of the 26th – 27th April. Here we have selected waves based on an amplitude threshold. This wave envelope is given in light grey shading around the wave packets. The wave is persistent across the time period and the area of influence increases.

292 **4.2 S-Transform Analysis - Example Results**

293 As described above, from the S-Transform we are able to extract wave amplitude,  
 294 horizontal wavelengths, frequency and period of each pixel in an image. This allows us  
 295 to build a picture of the waves and their properties as they vary over time.

296 Figure 5 presents an example of a single frame from the output of the 3D S-Transform  
 297 as applied to the airglow imager data over the night of the 26th – 27th April 2012. Fig-  
 298 ure 5a shows the input data, b the reconstructed wave field based on the output, c the  
 299 wave amplitude at each point on the image, d the horizontal wavelength calculated as  
 300 a Pythagorean sum of the wavelengths in the x and y directions, e the direction of prop-  
 301 agation and f the period in minutes. It can be seen from this example that the wave seen  
 302 in the input data and our above time-varying example is clearly detected by the anal-  
 303 ysis.

304 In Figure 5a, we can visually identify wave fronts in the image, which are clear to  
 305 the eye and free from major interference. This means that they are well-placed to be re-  
 306 covered by the S-Transform. A similar picture is seen in Figure 5b, where we reconstruct  
 307 the detected wave field reconstruction (as described by Hindley et al. (2016)). As this  
 308 field is visually and quantitatively similar to the input, we can be confident that the wave  
 309 properties we are calculating using the S-Transform are reliable. In Figure 5c we then  
 310 show the amplitude calculated for each pixel on the image. We see that the area with  
 311 more pronounced wave features marked with a black box in Figure 5a – d in the input  
 312 data exhibits stronger amplitudes than signals in the rest of the figure.

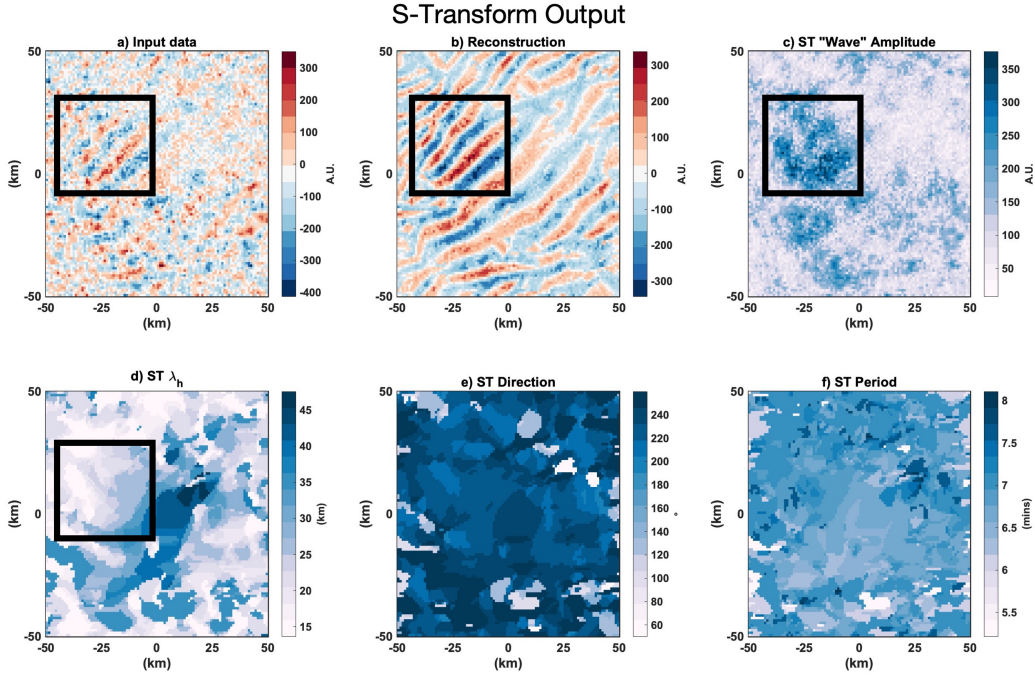


**Figure 5.** Examples of the S-Transform output. In panel a, the input data following the star and galaxy removal, b presents the reconstruction of the wave field given the wave properties, c shows the amplitude of the wave at each pixel, d presents the horizontal wavelength as a Pythagorean sum of the x and y directions, e direction propagation of the dominant wave at each pixel and f presents the period in minutes.

313 Further, we show the wavelength in the horizontal direction in Figure 5d. A brief  
 314 visual check shows that the long wavelengths present in the input data are picked  
 315 up by the S-Transform in the reconstruction and in this field. Finally, the periods are  
 316 shown in Figure 5f ranging from around 5 to 8 minutes. These are fast waves, as the Brunt-  
 317 Väisälä period at this height is around 5 minutes (Wüst et al., 2017).

### 318 4.3 S-Transform Analysis - All-Night Results

319 We now show integrated results over the entire night. Figure 6 presents histograms  
 320 of this output, as quantified at the voxel level. Specifically, we have defined this dataset  
 321 such that each voxel above the 90th percentile threshold used previously for Figure 4 con-  
 322 tributes a single count to each histogram. The histograms are defined across 15 equally-  
 323 sized bins, with the bin width calculated by computing the range between the maximum  
 324 and minimum values and dividing this range into 15 equal-width bins. Here we present  
 325 the horizontal wavelength  $\lambda_h$  in Figure 6a, the vertical wavelength  $\lambda_z$  in b, the angular  
 326 frequency  $\omega$  in c, the phase speed  $c_p$  in d, the group speed  $c_g$  in e, the direction in f, the  
 327 temporal period  $T$  in g, the intrinsic angular frequency  $\hat{\omega}$  in h, the intrinsic phase speed  
 328  $\hat{c}_p$  in i, and the intrinsic group speed  $\hat{c}_g$  in j.

329 The distribution of horizontal wavelengths seen in Figure 6a shows that measured  
 330 horizontal wavelengths are generally below 30 km. However, there is also a distinct peak  
 331 at wavelengths  $\sim 35$  km. This peak likely arises due to the histograms being computed  
 332 from voxel-level rather than wave-level data: such a feature is consistent with a promi-

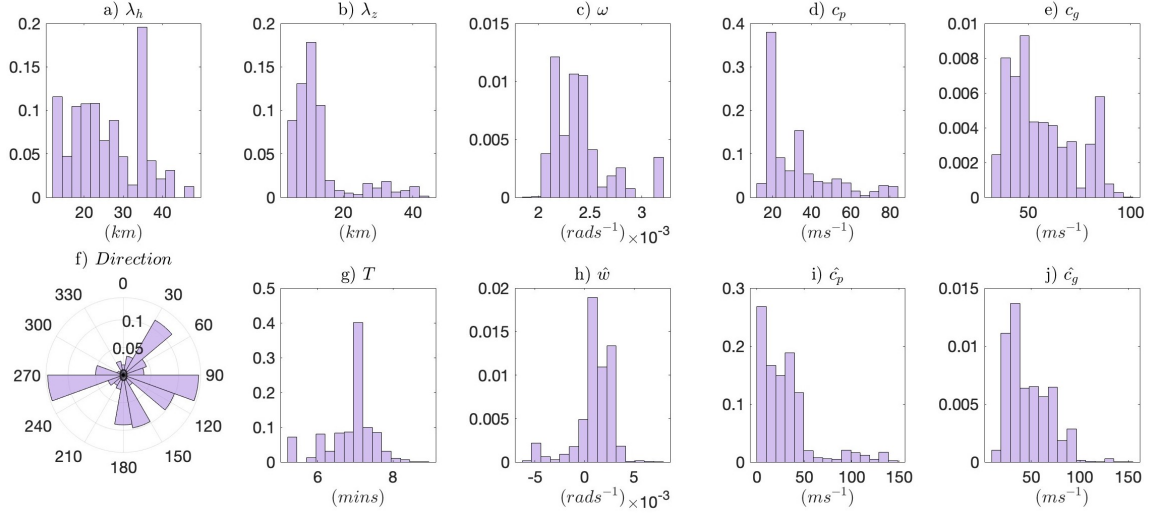


**Figure 6.** Histograms of the wave properties extracted from the airglow images using the 3D S-Transform for the night of 26th – 27th April 2012. Presented here are the horizontal wavelength  $\lambda_h$  in a), the vertical wavelength  $\lambda_z$  in b), the angular frequency  $\omega$  in c), the phase speed  $c_p$  in d), the group speed  $c_g$  in e), the direction in f), the temporal period  $T$  in g), the intrinsic angular frequency  $\hat{\omega}$  in h), the intrinsic phase speed  $\hat{c}_p$  in i), and the intrinsic group speed  $\hat{c}_g$  in j).

333      nent and persistent wave that lasts for multiple frames contributed a large number of counts  
 334      in this bin. If we had a method that counted a wave only once as it progressed over the  
 335      image, we would expect this peak to be less pronounced. However, defining the limits  
 336      of a wave packet within data of this type is a non-trivial exercise and developing a method  
 337      such as this is beyond the scope of this paper.

338      Vertical wavelengths in Figure 6b shows smaller wavelengths below 20 km are more  
 339      common than those above 20 km. We can see the peak of this distribution is around 16  
 340      km.

341      The angular frequencies computed for the waves, shown in Figure 6c, suggest a pref-  
 342      erence for values below  $2.5 \text{ rad s}^{-1}$ , but with a noticeable secondary peak apparent at  
 343      values  $\sim 3.1 \text{ rad s}^{-1}$ . In Figure 6d the phase speeds show a preference for lower speeds  
 344      with a peak at  $20 \text{ ms}^{-1}$  and at  $35 \text{ ms}^{-1}$ . We can see phase speeds of 15 to  $90 \text{ ms}^{-1}$ . Larger  
 345      speeds are, however, less common. The group speed in Figure 6e shows presents two peaks,  
 346      one at  $55 \text{ ms}^{-1}$  and one at  $90 \text{ ms}^{-1}$ . Group speeds between  $25 \text{ ms}^{-1}$  and  $75 \text{ ms}^{-1}$  are  
 347      more common than speeds between  $75 \text{ ms}^{-1}$  and  $100 \text{ ms}^{-1}$ , but both are still prominent.

348      Figure 6f presents the direction of the waves displayed as a bearing (clockwise from  
 349      north). We can see that some directions are more prominent, i.e. northeast, east-southeast  
 350      and west-southwest. There are also some waves travelling south.

351      We present the periods of the waves in Figure 6g where the most common period  
 352      is at 7 minutes, with periods from 5.5 mins to 8 mins also being present. Above 8 mins,  
 353      there are limited instances of waves present.

354      The following parameters are intrinsic wave parameters; that is, they are the wave  
 355      parameters from the frame of reference of the wind the wave propagates through. In Fig-  
 356      ure 6h, presenting intrinsic angular frequency, we can see an almost symmetrical distri-

357 bution surrounding  $0 \text{ rad s}^{-1}$  implying that in the wave frame of reference, waves are  
 358 travelling both with and against the wind. In Figure 6i, we present the intrinsic phase  
 359 speed where a preference for lower speeds is evident, specifically below  $50 \text{ ms}^{-1}$ . Speeds  
 360 between  $100 \text{ ms}^{-1}$  and  $150 \text{ ms}^{-1}$  are observed, but this is a very low occurrence. Finally,  
 361 intrinsic group speed shows an almost log-normal distribution with speeds between  $10$   
 362  $\text{ms}^{-1}$  and  $130 \text{ ms}^{-1}$  with a peak at around  $25 \text{ ms}^{-1}$ .

363 In Figure 6e, we observe group speeds which are large and non-zero. This implies  
 364 that the waves we see are not only travelling fast but horizontally propagating. This is  
 365 at odds with common GW parameterisations which consider GWs as being constrained  
 366 to the vertical column of a single gridbox and which can only propagate vertically within  
 367 this column (Alexander et al., 2010; Kalisch et al., 2014). These results provide further  
 368 evidence that this is not the case and that GW parameterisations which do not consider  
 369 horizontal propagation are unsuitable for capturing these small-scale waves which carry  
 370 significant quantities of energy and momentum (Geller et al., 2013; Alexander et al., 2010).

## 371 5 Discussion

372 Since in our study we apply a novel method, it is important to assess our results  
 373 properly in the context of previous work using more conventional approaches. Accord-  
 374 ingly, in this section we compare our results quantitatively to previous studies (section  
 375 5.1), before discussing the advantages and disadvantages of our approach relative to other  
 376 available methods (section 5.2).

### 377 5.1 Results Comparison to Previous Studies

378 We have found horizontal wavelengths ranging from around 5 to 45 km, with most  
 379 voxels being associated with values between 20 – 25 km. This compares favourably with  
 380 previous studies, which show wavelengths between 20 – 30 km (Kam et al., 2017; Pautet,  
 381 2005; Ejiri et al., 2003; Hecht et al., 2001; R. Stockwell et al., 1996), and with peaks at  
 382 35 km seen in (Hecht, 2002).

383 Nielsen et al. (2009) investigated GWs in the hydroxyl airglow layer, using data  
 384 from when the same imaging system used in our study was deployed instead to the British  
 385 Antarctic Survey base at Halley, Antarctica ( $76^\circ\text{S}$ ,  $27^\circ\text{W}$ ). They investigated the sea-  
 386 sonal climatology of individual quasi-monochromatic, short-period gravity-wave char-  
 387 acteristics at high-southern latitudes. These characteristics were observed over the 2000  
 388 and 2001 austral winter seasons. They found horizontal wavelengths from 10 – 70 km,  
 389 producing a log-normal distribution with a peak at 15 – 20 km. Comparatively, we have  
 390 observed a range of 10 – 50 km with a high count at 35 km. As we test only a single night  
 391 of data, this difference may simply be due to the most dominant wave on this specific  
 392 night having this wavelength. As the S-Transform gives us voxel-level information, not  
 393 individual wave events, we cannot say how many waves had this wavelength with this  
 394 information alone.

395 Similarly, for observed wave periods, we see a range of values from 5 – 9  $\text{ms}^{-1}$  with  
 396 a peak at around  $7.5 \text{ ms}^{-1}$ . Nielsen et al. (2009) found a range of 5 – 30  $\text{ms}^{-1}$  with a  
 397 log-normal distribution with peak at  $\sim 7.5 \text{ ms}^{-1}$ . This is broadly similar to the peak we  
 398 have seen, which suggests that this is a common wave period. The wide range of peri-  
 399 ods seen in their study will come from the two winters of data that have been used. We  
 400 have used one night to benchmark our method resulting, therefore, in less data and fewer  
 401 wave events.

402 The directions observed by Nielsen et al. (2009) showed a clear preference for prop-  
 403 agation towards the South Pole, and there is limited evidence of waves propagating North.

404 Similarly, we have shown that propagation southwards is apparent in our case; however,  
405 the directions we observed also peak significantly in the WSW and ESE directions.

406 Kam et al. (2017) observed a very similar range of observed phase speeds as in our  
407 study; however, the periods we observe are faster, with a range from 5 – 9 minutes com-  
408 pared with the range of 5 – 60 minutes in the work of Kam et al. (2017). This also sug-  
409 gests that the results we have uncovered using the 3DST are plausible.

410 With observed phase speed, Nielsen et al. (2009) saw a range from 0 to 100  $\text{ms}^{-1}$   
411 with a peak at 30 to 40  $\text{ms}^{-1}$ . This is an almost Gaussian distribution. We observe a  
412 range from 10 to 90  $\text{ms}^{-1}$ , very similar to that observed at Halley. We also observed a  
413 peak at 20  $\text{ms}^{-1}$ . This could be a persistent wave event that was spatially large and there-  
414 fore could be present over many voxels.

## 415 5.2 Methodological Comparisons

416 The addition of supporting meteor radar data also allows us to convert these pa-  
417 rameters from the ground-based to the intrinsic frame.

### 418 5.2.1 The 2D Stockwell Transform

419 Here, we apply the 3D Stockwell Transform to data of this type for the first time.  
420 The simpler two-dimensional S-Transform (2DST) has however previously been applied  
421 to airglow data. Specifically, R. G. Stockwell and Lowe (2001) applied the 2DST to 16  
422 x 16 pixel airglow images, covering a field of view of 1.5 km at the height of the airglow  
423 at 87 km. In addition to accounting for time variation, advances in computing power also  
424 allow us to work at a much larger scale, allowing us to apply the technique to a full night  
425 of observations totalling 360 frames, each of 101 by 101 pixels and hence covering an area  
426 of sky equivalent to 100 by 100 km on the surface.

427 This combination of features allows us to quantify wave parameters over a much  
428 larger field of view than (R. G. Stockwell & Lowe, 2001), and to measure many additional  
429 parameters. In particular, the ability to simultaneously obtain both spatial information  
430 and the temporal frequency of these waves and how they covary is a key advantage over  
431 this older 2D approach.

### 432 5.2.2 The Fast Fourier Transform

433 An alternative approach is to use just a 3D FFT without the additional window-  
434 ing properties of the ST. This is computationally very significantly cheaper. As an ex-  
435 ample of this approach, Rourke et al. (2017) investigated short-period GWs and ripples  
436 at Davis Station, Antarctica (68 °S, 78 °E) using a scanning radiometer to measure hy-  
437 droxyl airglow perturbations.

438 The approach of Rourke et al. (2017) identified the dominant wave feature in each  
439 frame using the FFT, with the period of the dominant wave determined from time-variations  
440 in the FFTs of the weighted centre of 32 successive images centred on the frame in ques-  
441 tion. Using a sampling rate of 1 min and a maximum window length of 32, the range  
442 of wave periods detectable by this approach was 2 to 16 minutes. They then used lag  
443 analysis to determine the wave direction and speed.

444 Our method provides similar outputs, but whereas their approach gave results at  
445 the frame level our 3DST approach allows the measurement of geographically-decomposed  
446 parameters at the single-voxel level. This allows for more information to be extracted  
447 about the waves, and for multiple waves in the same panel to be measured.

448

### 5.2.3 Cospectral Analysis

449

450

451

Another method of extracting wave properties is co-spectral analysis, as applied by e.g. Cao and Liu (2022) to airglow images observed at Andes Lidar Observatory (30.3 °S, 70.7 °W) in northern Chile.

452

453

454

455

456

457

458

459

460

In this study, images were unwrapped to a flat field to account for the van Rhijn effect. They removed the galaxy using the Principal Component Analysis (PCA) method from Z. Li et al. (2014), then used three consecutive images to create two time-differenced images. Horizontal wave properties such as wavelength, observed phase speed, direction and relative emission perturbation amplitude were then derived from the co-spectra of the two images, supported as in our study by background winds from a SKiYMET meteor radar system based at the Andes Lidar Observatory to convert between the intrinsic and ground-based frames. Once this step was performed, any wavelengths below 10 km and any periods below the buoyancy frequency were removed.

461

462

463

464

465

466

This method, similar to our 3DST, allowed both observed and intrinsic parameters can be established along with relative emission amplitudes of consecutive images. However, the method also results in some lost information due to taking the direct differences between each frame. Furthermore, it also assumes that the phase difference from voxel to voxel in time is accurate; therefore, any noise present (very likely in real observations) will impact significantly and directly upon the quality of the final results.

467

### 5.2.4 The M-Transform

468

469

470

The final method we discuss is the M-Transform. This was formulated by Matsuda et al. (2014) as a 3D method to extract wave properties, similar in underlying conception to the S-Transform.

471

472

473

474

475

476

477

As with the S-Transform, the M-Transform requires a time series of airglow images with fixed and consistent pixel time spacing. For this method, once again, the airglow images must be preprocessed to remove stars, the galaxy, and any lens effects, and must also be projected onto geographic coordinates. Once this has been done, the M-transform transforms the Power Spectral Density (PSD) in the wavenumber domain ( $k, l, \omega$ ), where  $k$  and  $l$  are the wavenumbers in the zonal and meridional direction, respectively and  $\omega$  is the frequency in the phase velocity domain ( $v_x, v_y, \omega$ ) via the following equations:

$$v_x = \frac{\omega k}{k^2 + l^2} \quad (12)$$

$$v_y = \frac{\omega l}{k^2 + l^2} \quad (13)$$

478

479

Where  $v_x$  and  $v_y$  are the orthogonal projections of the phase velocity onto zonal and meridional axes, respectively. This allows for the calculation of phase speed and azimuth as:

$$(v_x, v_y) = c(\sin\phi, \cos\phi) \quad (14)$$

480

481

Where  $c$  is the phase speed, and  $\phi$  is the azimuth. Finally, the phase velocity is integrated to give a 2D phase velocity spectrum.

482

483

484

485

486

487

488

The M-transform shares many benefits with the S-Transform method we present in this study. For instance, it is highly automated and does not require interaction with the user, it is 3D, and it provides many wave properties directly. However, the M-transform is statistical, and there is no information provided from the analysis about specific locations and times within the dataset used - all properties are measured at the bulk level for the whole dataset. The ability of the S-Transform approach to resolve the same properties at the voxel level is thus a significant advantage.

## 6 Conclusions

In this study, we have presented a new application of a 3D spectral analysis technique, the 3D S-Transform, to airglow imager data from the Antarctic Peninsula at the British Antarctic Survey Base at Rothera (68°S, 68°W).

The method is automated and can identify wave properties for each pixel; we can, therefore, use it to investigate the spatial extent of the wave, as in Figure 4.

We have found that:

1. The 3D S-Transform method works well with processed airglow imager data and measures wave parameters consistent with the airglow literature
2. The majority of waves seen in the airglow in this case study are small, fast GWs with short periods.
3. We see a distribution of horizontal wavelengths between 10 to 50 km with a sharp peak at 35 km, possibly due to methodological reasons
4. Vertical wavelengths peak at values below 20 km, peaking at around 15 km but with the largest peak at around 40 km.
5. Phase speeds are generally low, and group speeds are high and non-zero This suggests that the waves observed are travelling horizontally and also fast, further suggesting that GW parametrisations which do not account for horizontal movement are inadequate
6. Finally, we can give accurate locations of where the waves in the airglow are present due to the 3D S-Transform investigating waves on the pixel rather than wave event level.

Future studies could advantageously use the S-Transform in tandem with an automated image processing technique to improve the process thus allowing the identification of airglow images that are of sufficient clarity for use in the investigation of GWs. Used together, these processes would allow airglow images to be processed and analysed in one programme with little input from the user, allowing for a fully automated process. This would result in GW parameters and their locations on each frame. More work on the spatial extent of the wave could then be performed and investigated.

## Data Availability

The meteor radar data used in this study are archived as part of from Mitchell, N. (2019): University of Bath: Rothera Skymet Meteor Radar data (2005 – present). Centre for Environmental Data Analysis, 2022. <https://catalogue.ceda.ac.uk/uuid/aa44e02718fd4ba49cefe36d884c6e>

## Acknowledgments

SMD is supported by a NERC GW4+ Doctoral Training Partnership studentship from the Natural Environment Research Council (NERC, grant number NE/L002434/1). TMG, CJW and NJM are supported by NERC (NE/R001391/1 and NE/R001235/1) and CJW by a Royal Society University Research Fellowship (URF\R\221023)

## CRedit authorship contribution statement

Conceptualisation: CJW and NJM; Data curation: SMD, NPH, TM-G, P-DP and MJT; Formal analysis: SMD and NPH; Investigation: SMD and NPH; Methodology: SMD, NPH, CJW and NJM; Project administration: CJW; Resources: CJW, NJM and TM-G; Software: SMD and NPH; Supervision: CJW, NJM and TM-G; Validation: NPH, CJW, NJM and TM-G; Visualization: SMD and CJW; Writing – original draft: SMD; Writing - review and editing: SMD, NPH, CJW and TM-G.

534

**References**

535

536

537

538

539

540

541

542

543

544

545

546

547

548

549

550

551

552

553

554

555

556

557

558

559

560

561

562

563

564

565

566

567

568

569

570

571

572

573

574

575

576

577

578

579

580

581

582

583

584

585

586

587

588

- Alexander, M. J., Geller, M., McLandress, C., Polavarapu, S., Preusse, P., Sassi, F., ... Watanabe, S. (2010, July). Recent developments in gravity-wave effects in climate models and the global distribution of gravity-wave momentum flux from observations and models. *Quarterly Journal of the Royal Meteorological Society*, *136*(650), 1103–1124. Retrieved from <https://doi.org/10.1002/qj.637> doi: 10.1002/qj.637
- Alexander, M. J., & Teitelbaum, H. (2007, November). Observation and analysis of a large amplitude mountain wave event over the antarctic peninsula. *Journal of Geophysical Research*, *112*(D21). Retrieved from <https://doi.org/10.1029/2006jd008368> doi: 10.1029/2006jd008368
- Baker, D. J., & Stair, A. T. (1988, April). Rocket measurements of the altitude distributions of the hydroxyl airglow. *Physica Scripta*, *37*(4), 611–622. Retrieved from <https://doi.org/10.1088/0031-8949/37/4/021> doi: 10.1088/0031-8949/37/4/021
- Baumgaertner, A. J. G., & McDonald, A. J. (2007, March). A gravity wave climatology for antarctica compiled from challenging minisatellite payload/global positioning system (CHAMP/GPS) radio occultations. *Journal of Geophysical Research*, *112*(D5). Retrieved from <https://doi.org/10.1029/2006jd007504> doi: 10.1029/2006jd007504
- Becker, E. (2012, October). Dynamical control of the middle atmosphere. *Space Science Reviews*, *168*(1-4), 283–314. Retrieved from <https://doi.org/10.1007/s11214-011-9841-5> doi: 10.1007/s11214-011-9841-5
- Beldon, C., Muller, H., & Mitchell, N. (2006, March). The 8-hour tide in the mesosphere and lower thermosphere over the UK, 1988–2004. *Journal of Atmospheric and Solar-Terrestrial Physics*, *68*(6), 655–668. Retrieved from <https://doi.org/10.1016/j.jastp.2005.10.004> doi: 10.1016/j.jastp.2005.10.004
- Cao, B., & Liu, A. Z. (2016, January). Intermittency of gravity wave momentum flux in the mesopause region observed with an all-sky airglow imager. *Journal of Geophysical Research: Atmospheres*, *121*(2), 650–663. Retrieved from <https://doi.org/10.1002/2015jd023802> doi: 10.1002/2015jd023802
- Cao, B., & Liu, A. Z. (2022, June). Statistical characteristics of high-frequency gravity waves observed by an airglow imager at andes lidar observatory. *Earth and Space Science*, *9*(6). Retrieved from <https://doi.org/10.1029/2022ea002256> doi: 10.1029/2022ea002256
- Davis, R. N., Du, J., Smith, A. K., Ward, W. E., & Mitchell, N. J. (2013, September). The diurnal and semidiurnal tides over ascension island (° s, 14° w) and their interaction with the stratospheric quasi-biennial oscillation: studies with meteor radar, eCMAM and WACCM. *Atmospheric Chemistry and Physics*, *13*(18), 9543–9564. Retrieved from <https://doi.org/10.5194/acp-13-9543-2013> doi: 10.5194/acp-13-9543-2013
- Dempsey, S. M., Hindley, N. P., Moffat-Griffin, T., Wright, C. J., Smith, A. K., Du, J., & Mitchell, N. J. (2021, January). Winds and tides of the antarctic mesosphere and lower thermosphere: One year of meteor-radar observations over rothera (68°s, 68°w) and comparisons with WACCM and eCMAM. *Journal of Atmospheric and Solar-Terrestrial Physics*, *212*, 105510. Retrieved from <https://doi.org/10.1016/j.jastp.2020.105510> doi: 10.1016/j.jastp.2020.105510
- Ejiri, M. K., Shiokawa, K., Ogawa, T., Igarashi, K., Nakamura, T., & Tsuda, T. (2003, November). Statistical study of short-period gravity waves in OH and OI nightglow images at two separated sites. *Journal of Geophysical Research: Atmospheres*, *108*(D21). Retrieved from <https://doi.org/10.1029/2002jd002795> doi: 10.1029/2002jd002795
- Fritts, D. C., & Alexander, M. J. (2003, March). Gravity wave dynamics and ef-

- 589       fects in the middle atmosphere. *Reviews of Geophysics*, 41(1). Retrieved from  
590       <https://doi.org/10.1029/2001rg000106> doi: 10.1029/2001rg000106
- 591       Fritts, D. C., Vadas, S. L., Wan, K., & Werne, J. A. (2006, February). Mean  
592       and variable forcing of the middle atmosphere by gravity waves. *Journal of Atmospheric and Solar-Terrestrial Physics*, 68(3-5), 247–265. Re-  
593       trieved from <https://doi.org/10.1016/j.jastp.2005.04.010> doi:  
594       10.1016/j.jastp.2005.04.010
- 595  
596       Ganaie, B. A., Ramkumar, T., Bhat, A. H., & Malik, M. A. (2022, July). Im-  
597       ager observation of concentric mesospheric gravity waves over srinagar,  
598       jammu and kashmir, india. *Advances in Space Research*, 70(2), 427–439.  
599       Retrieved from <https://doi.org/10.1016/j.asr.2022.04.035> doi:  
600       10.1016/j.asr.2022.04.035
- 601       Gardner, C. S., & Taylor, M. J. (1998). Observational limits for lidar, radar,  
602       and airglow imager measurements of gravity wave parameters. *Journal of*  
603       *Geophysical Research: Atmospheres*, 103(D6), 6427–6437. Retrieved from  
604       <https://agupubs.onlinelibrary.wiley.com/doi/abs/10.1029/97JD03378>  
605       doi: <https://doi.org/10.1029/97JD03378>
- 606       Geller, M. A., Alexander, M. J., Love, P. T., Bacmeister, J., Ern, M., Hertzog, A.,  
607       ... Zhou, T. (2013, August). A comparison between gravity wave momentum  
608       fluxes in observations and climate models. *Journal of Climate*, 26(17), 6383–  
609       6405. Retrieved from <https://doi.org/10.1175/jcli-d-12-00545.1> doi:  
610       10.1175/jcli-d-12-00545.1
- 611       Goldberg, R. A. (2004). The MaCWAVE/MIDAS rocket and ground-based measure-  
612       ments of polar summer dynamics: Overview and mean state structure. *Geo-*  
613       *physical Research Letters*, 31(24). Retrieved from <https://doi.org/10.1029/2004gl019411> doi: 10.1029/2004gl019411
- 614  
615       Hecht, J. H. (2002). An observation of a fast external atmospheric acoustic-gravity  
616       wave. *Journal of Geophysical Research*, 107(D20). Retrieved from [https://](https://doi.org/10.1029/2001jd001438)  
617       [doi.org/10.1029/2001jd001438](https://doi.org/10.1029/2001jd001438) doi: 10.1029/2001jd001438
- 618       Hecht, J. H., Walterscheid, R. L., Hickey, M. P., & Franke, S. J. (2001, March).  
619       Climatology and modeling of quasi-monochromatic atmospheric gravity  
620       waves observed over urbana illinois. *Journal of Geophysical Research: At-*  
621       *mospheres*, 106(D6), 5181–5195. Retrieved from <https://doi.org/10.1029/2000jd900722> doi: 10.1029/2000jd900722
- 622  
623       Hindley, N. P., Cobbett, N., Fritts, D. C., Janchez, D., Mitchell, N. J., Moffat-  
624       Griffin, T., ... Wright, C. J. (2022, December). Radar observations of winds,  
625       waves and tides in the mesosphere and lower thermosphere over south georgia  
626       island (54°s, 36°w) and comparison to WACCM simulations. *ACP*. Retrieved  
627       from <https://doi.org/10.5194/acp-2021-981> doi: 10.5194/acp-2021-981
- 628       Hindley, N. P., Smith, N. D., Wright, C. J., Rees, D. A. S., & Mitchell, N. J. (2016,  
629       June). A two-dimensional stockwell transform for gravity wave analysis of  
630       AIRS measurements. *Atmospheric Measurement Techniques*, 9(6), 2545–  
631       2565. Retrieved from <https://doi.org/10.5194/amt-9-2545-2016> doi:  
632       10.5194/amt-9-2545-2016
- 633       Hindley, N. P., Wright, C. J., Smith, N. D., Hoffmann, L., Holt, L. A., Alexander,  
634       M. J., ... Mitchell, N. J. (2019, December). Gravity waves in the winter  
635       stratosphere over the southern ocean: high-resolution satellite observations and  
636       3-d spectral analysis. *Atmospheric Chemistry and Physics*, 19(24), 15377–  
637       15414. Retrieved from <https://doi.org/10.5194/acp-19-15377-2019> doi:  
638       10.5194/acp-19-15377-2019
- 639       Hindley, N. P., Wright, C. J., Smith, N. D., & Mitchell, N. J. (2015, July). The  
640       southern stratospheric gravity wave hot spot: individual waves and their mo-  
641       mentum fluxes measured by COSMIC GPS-RO. *Atmospheric Chemistry and*  
642       *Physics*, 15(14), 7797–7818. Retrieved from [https://doi.org/10.5194/](https://doi.org/10.5194/acp-15-7797-2015)  
643       [acp-15-7797-2015](https://doi.org/10.5194/acp-15-7797-2015) doi: 10.5194/acp-15-7797-2015

- 644 Hocking, W., Fuller, B., & Vandeppeer, B. (2001, January). Real-time determi-  
 645 nation of meteor-related parameters utilizing modern digital technology.  
 646 *Journal of Atmospheric and Solar-Terrestrial Physics*, *63*(2-3), 155–169.  
 647 Retrieved from [https://doi.org/10.1016/s1364-6826\(00\)00138-3](https://doi.org/10.1016/s1364-6826(00)00138-3) doi:  
 648 10.1016/s1364-6826(00)00138-3
- 649 Hu, S., Ma, S., Yan, W., Hindley, N. P., Xu, K., & Jiang, J. (2019a, January).  
 650 Measuring gravity wave parameters from a nighttime satellite low-light im-  
 651 age based on two-dimensional stockwell transform. *Journal of Atmospheric*  
 652 *and Oceanic Technology*, *36*(1), 41–51. Retrieved from [https://doi.org/](https://doi.org/10.1175/jtech-d-18-0092.1)  
 653 [10.1175/jtech-d-18-0092.1](https://doi.org/10.1175/jtech-d-18-0092.1) doi: 10.1175/jtech-d-18-0092.1
- 654 Hu, S., Ma, S., Yan, W., Hindley, N. P., Xu, K., & Jiang, J. (2019b, January).  
 655 Measuring gravity wave parameters from a nighttime satellite low-light im-  
 656 age based on two-dimensional stockwell transform. *Journal of Atmospheric*  
 657 *and Oceanic Technology*, *36*(1), 41–51. Retrieved from [https://doi.org/](https://doi.org/10.1175/jtech-d-18-0092.1)  
 658 [10.1175/jtech-d-18-0092.1](https://doi.org/10.1175/jtech-d-18-0092.1) doi: 10.1175/jtech-d-18-0092.1
- 659 Hu, S., Ma, S., Yan, W., Hindley, N. P., & Zhao, X. (2019, April). Measuring inter-  
 660 nal solitary wave parameters based on VIIRS/DNB data. *International Jour-*  
 661 *nal of Remote Sensing*, *40*(20), 7805–7816. Retrieved from [https://doi.org/](https://doi.org/10.1080/01431161.2019.1608389)  
 662 [10.1080/01431161.2019.1608389](https://doi.org/10.1080/01431161.2019.1608389) doi: 10.1080/01431161.2019.1608389
- 663 Kalisch, S., Preusse, P., Ern, M., Eckermann, S. D., & Riese, M. (2014). Differences  
 664 in gravity wave drag between realistic oblique and assumed vertical propaga-  
 665 tion. *Journal of Geophysical Research: Atmospheres*, *119*(17), 10,081–10,099.  
 666 Retrieved from [https://agupubs.onlinelibrary.wiley.com/doi/abs/](https://agupubs.onlinelibrary.wiley.com/doi/abs/10.1002/2014JD021779)  
 667 [10.1002/2014JD021779](https://doi.org/10.1002/2014JD021779) doi: <https://doi.org/10.1002/2014JD021779>
- 668 Kam, H., Jee, G., Kim, Y., bae Ham, Y., & Song, I-S. (2017, March). Statisti-  
 669 cal analysis of mesospheric gravity waves over king sejong station, antarctica  
 670 (62.2°s, 58.8°w). *Journal of Atmospheric and Solar-Terrestrial Physics*, *155*,  
 671 86–94. Retrieved from <https://doi.org/10.1016/j.jastp.2017.02.006>  
 672 doi: 10.1016/j.jastp.2017.02.006
- 673 Khomich, V. Y., Semenov, A. I., & Shefov, N. N. (2008). *Airglow as an indicator*  
 674 *of upper atmospheric structure and dynamics*. Springer Science & Business Me-  
 675 dia.
- 676 Kogure, M., Yue, J., & Liu, H. (2021, April). Gravity wave weakening during  
 677 the 2019 antarctic stratospheric sudden warming. *Geophysical Research Let-*  
 678 *ters*, *48*(8). Retrieved from <https://doi.org/10.1029/2021gl092537> doi:  
 679 10.1029/2021gl092537
- 680 Kogure, M., Yue, J., Nakamura, T., Hoffmann, L., Vadas, S. L., Tomikawa, Y.,  
 681 ... Janches, D. (2020, September). First direct observational evidence for  
 682 secondary gravity waves generated by mountain waves over the andes. *Geo-*  
 683 *physical Research Letters*, *47*(17). Retrieved from [https://doi.org/10.1029/](https://doi.org/10.1029/2020gl088845)  
 684 [2020gl088845](https://doi.org/10.1029/2020gl088845) doi: 10.1029/2020gl088845
- 685 Li, J., Li, T., Dou, X., Fang, X., Cao, B., She, C.-Y., ... Thorsen, D. (2017, March).  
 686 Characteristics of ripple structures revealed in OH airglow images. *Journal*  
 687 *of Geophysical Research: Space Physics*, *122*(3), 3748–3759. Retrieved from  
 688 <https://doi.org/10.1002/2016ja023538> doi: 10.1002/2016ja023538
- 689 Li, Z., Liu, A., & Sivjee, G. G. (2014, April). Removing milky way from airglow  
 690 images using principal component analysis. *Journal of Atmospheric and*  
 691 *Solar-Terrestrial Physics*, *110-111*, 50–57. Retrieved from [https://doi.org/](https://doi.org/10.1016/j.jastp.2014.01.016)  
 692 [10.1016/j.jastp.2014.01.016](https://doi.org/10.1016/j.jastp.2014.01.016) doi: 10.1016/j.jastp.2014.01.016
- 693 Li, Z., Liu, A. Z., Lu, X., Swenson, G. R., & Franke, S. J. (2011, November).  
 694 Gravity wave characteristics from OH airglow imager over maui. *Journal*  
 695 *of Geophysical Research: Atmospheres*, *116*(D22), n/a–n/a. Retrieved from  
 696 <https://doi.org/10.1029/2011jd015870> doi: 10.1029/2011jd015870
- 697 Lindzen, R. S. (1981). Turbulence and stress owing to gravity wave and tidal  
 698 breakdown. *Journal of Geophysical Research*, *86*(C10), 9707. Retrieved from

- 699 <https://doi.org/10.1029/jc086ic10p09707> doi: 10.1029/jc086ic10p09707  
700 Matsuda, T. S., Nakamura, T., Ejiri, M. K., Tsutsumi, M., & Shiokawa, K. (2014,  
701 August). New statistical analysis of the horizontal phase velocity distri-  
702 bution of gravity waves observed by airglow imaging. *Journal of Geo-*  
703 *physical Research: Atmospheres*, *119*(16), 9707–9718. Retrieved from  
704 <https://doi.org/10.1002/2014jd021543> doi: 10.1002/2014jd021543
- 705 McDonald, A. J. (2012, August). Gravity wave occurrence statistics derived from  
706 paired COSMIC/FORMOSAT3 observations. *Journal of Geophysical Research:*  
707 *Atmospheres*, *117*(D15), n/a–n/a. Retrieved from [https://doi.org/10.1029/](https://doi.org/10.1029/2011jd016715)  
708 [2011jd016715](https://doi.org/10.1029/2011jd016715) doi: 10.1029/2011jd016715
- 709 Meinel, I. A. B. (1950, May). OH emission bands in the spectrum of the night  
710 sky. *The Astrophysical Journal*, *111*, 555. Retrieved from [https://doi.org/](https://doi.org/10.1086/145296)  
711 [10.1086/145296](https://doi.org/10.1086/145296) doi: 10.1086/145296
- 712 Miller, S. D., Straka, W. C., Yue, J., Smith, S. M., Alexander, M. J., Hoffmann,  
713 L., ... Partain, P. T. (2015, November). Upper atmospheric gravity wave  
714 details revealed in nightglow satellite imagery. *Proceedings of the National*  
715 *Academy of Sciences*, *112*(49). Retrieved from [https://doi.org/10.1073/](https://doi.org/10.1073/pnas.1508084112)  
716 [pnas.1508084112](https://doi.org/10.1073/pnas.1508084112) doi: 10.1073/pnas.1508084112
- 717 Mitchell, N. J. (2002). Mean winds and tides in the arctic mesosphere and lower  
718 thermosphere. *Journal of Geophysical Research*, *107*(A1). Retrieved from  
719 <https://doi.org/10.1029/2001ja900127> doi: 10.1029/2001ja900127
- 720 Moffat-Griffin, T., & Colwell, S. R. (2017, September). The characteristics of  
721 the lower stratospheric gravity wavefield above halley (75°s, 26°w), antar-  
722 tica, from radiosonde observations. *Journal of Geophysical Research: Atmo-*  
723 *spheres*, *122*(17), 8998–9010. Retrieved from [https://doi.org/10.1002/](https://doi.org/10.1002/2017jd027079)  
724 [2017jd027079](https://doi.org/10.1002/2017jd027079) doi: 10.1002/2017jd027079
- 725 Nielsen, K. (2007). *Climatology and case studies of mesospheric gravity waves ob-*  
726 *erved at polar latitudes*. Utah State University.
- 727 Nielsen, K., Taylor, M., Hibbins, R., & Jarvis, M. (2009, June). Climatology of  
728 short-period mesospheric gravity waves over halley, antarctica (76°s, 27°w).  
729 *Journal of Atmospheric and Solar-Terrestrial Physics*, *71*(8-9), 991–1000.  
730 Retrieved from <https://doi.org/10.1016/j.jastp.2009.04.005> doi:  
731 [10.1016/j.jastp.2009.04.005](https://doi.org/10.1016/j.jastp.2009.04.005)
- 732 Nielsen, K., Taylor, M. J., Pautet, P.-D., Fritts, D. C., Mitchell, N., Beldon, C.,  
733 ... Goldberg, R. A. (2006, July). Propagation of short-period gravity waves  
734 at high-latitudes during the MaCWAVE winter campaign. *Annales Geo-*  
735 *physicae*, *24*(4), 1227–1243. Retrieved from [https://doi.org/10.5194/](https://doi.org/10.5194/angeo-24-1227-2006)  
736 [angeo-24-1227-2006](https://doi.org/10.5194/angeo-24-1227-2006) doi: 10.5194/angeo-24-1227-2006
- 737 Pautet, P.-D. (2005). Climatology of short-period gravity waves observed over  
738 northern australia during the darwin area wave experiment (DAWEX)  
739 and their dominant source regions. *Journal of Geophysical Research*,  
740 *110*(D3). Retrieved from <https://doi.org/10.1029/2004jd004954> doi:  
741 [10.1029/2004jd004954](https://doi.org/10.1029/2004jd004954)
- 742 Perrett, J. A., Wright, C. J., Hindley, N. P., Hoffmann, L., Mitchell, N. J., Preusse,  
743 P., ... Eckermann, S. D. (2021, January). Determining gravity wave  
744 sources and propagation in the southern hemisphere by ray-tracing AIRS  
745 measurements. *Geophysical Research Letters*, *48*(2). Retrieved from  
746 <https://doi.org/10.1029/2020gl088621> doi: 10.1029/2020gl088621
- 747 Peterson, A. W. (1979, Oct). Airglow events visible to the naked eye. *Appl.*  
748 *Opt.*, *18*(20), 3390–3393. Retrieved from [http://opg.optica.org/ao/](http://opg.optica.org/ao/abstract.cfm?URI=ao-18-20-3390)  
749 [abstract.cfm?URI=ao-18-20-3390](http://opg.optica.org/ao/abstract.cfm?URI=ao-18-20-3390) doi: 10.1364/AO.18.003390
- 750 Rourke, S., Mulligan, F. J., French, W. J. R., & Murphy, D. J. (2017). A clima-  
751 tological study of short-period gravity waves and ripples at davis station,  
752 antarctica (68°s, 78°e), during the (austral winter february–october) period  
753 1999–2013. *Journal of Geophysical Research: Atmospheres*, *122*(21), 11,388–

- 754 11,404. Retrieved from <https://agupubs.onlinelibrary.wiley.com/doi/abs/10.1002/2017JD026998> doi: <https://doi.org/10.1002/2017JD026998>
- 755
- 756 Sedlak, R., Zuhr, A., Schmidt, C., Wüst, S., Bittner, M., Didebulidze, G. G., &  
757 Price, C. (2020, September). Intra-annual variations of spectrally re-  
758 solved gravity wave activity in the upper mesosphere/lower thermosphere  
759 (UMLT) region. *Atmospheric Measurement Techniques*, *13*(9), 5117–  
760 5128. Retrieved from <https://doi.org/10.5194/amt-13-5117-2020> doi:  
761 10.5194/amt-13-5117-2020
- 762 Stober, G., Kuchar, A., Pokhotelov, D., Liu, H., Liu, H.-L., Schmidt, H., ...  
763 Mitchell, N. (2021, September). Interhemispheric differences of meso-  
764 sphere–lower thermosphere winds and tides investigated from three whole-  
765 atmosphere models and meteor radar observations. *Atmospheric Chem-  
766 istry and Physics*, *21*(18), 13855–13902. Retrieved from <https://doi.org/10.5194/acp-21-13855-2021> doi:  
767 10.5194/acp-21-13855-2021
- 768 Stockwell, R., Mansinha, L., & Lowe, R. (1996). Localization of the complex spec-  
769 trum: the s transform. *IEEE Transactions on Signal Processing*, *44*(4), 998–  
770 1001. doi: 10.1109/78.492555
- 771 Stockwell, R. G., & Lowe, R. P. (2001, August). Airglow imaging of gravity waves:  
772 1. results from a small network of OH nightglow scanning imagers. *Journal of  
773 Geophysical Research: Atmospheres*, *106*(D15), 17185–17203. Retrieved from  
774 <https://doi.org/10.1029/2001jd900035> doi: 10.1029/2001jd900035
- 775 Takahashi, H., Melo, S. M. L., Clemesha, B. R., Simonich, D. M., Stegman, J., &  
776 Witt, G. (1996, February). Atomic hydrogen and ozone concentrations derived  
777 from simultaneous lidar and rocket airglow measurements in the equatorial re-  
778 gion. *Journal of Geophysical Research: Atmospheres*, *101*(D2), 4033–4040. Re-  
779 trieved from <https://doi.org/10.1029/95jd03035> doi: 10.1029/95jd03035
- 780 Taylor, M. J., Pendleton, W. R., Clark, S., Takahashi, H., Gobbi, D., & Goldberg,  
781 R. A. (1997, November). Image measurements of short-period gravity waves at  
782 equatorial latitudes. *Journal of Geophysical Research: Atmospheres*, *102*(D22),  
783 26283–26299. Retrieved from <https://doi.org/10.1029/96jd03515> doi:  
784 10.1029/96jd03515
- 785 Taylor, M. J., Ryan, E. H., Tuan, T. F., & Edwards, R. (1993, April). Evidence  
786 of preferential directions for gravity wave propagation due to wind filtering  
787 in the middle atmosphere. *Journal of Geophysical Research: Space Physics*,  
788 *98*(A4), 6047–6057. Retrieved from <https://doi.org/10.1029/92ja02604>  
789 doi: 10.1029/92ja02604
- 790 von Savigny, C. (2015, May). Variability of OH(3–1) emission altitude from 2003  
791 to 2011: Long-term stability and universality of the emission rate–altitude  
792 relationship. *Journal of Atmospheric and Solar-Terrestrial Physics*, *127*, 120–  
793 128. Retrieved from <https://doi.org/10.1016/j.jastp.2015.02.001> doi:  
794 10.1016/j.jastp.2015.02.001
- 795 Wright, C. J., & Gille, J. C. (2013, May). Detecting overlapping gravity waves us-  
796 ing the s-transform. *Geophysical Research Letters*, *40*(9), 1850–1855. Retrieved  
797 from <https://doi.org/10.1002/grl.50378> doi: 10.1002/grl.50378
- 798 Wright, C. J., Hindley, N. P., Hoffmann, L., Alexander, M. J., & Mitchell, N. J.  
799 (2017, July). Exploring gravity wave characteristics in 3-d using a novel  
800 s-transform technique: AIRS/aqua measurements over the southern andes  
801 and drake passage. *Atmospheric Chemistry and Physics*, *17*(13), 8553–  
802 8575. Retrieved from <https://doi.org/10.5194/acp-17-8553-2017> doi:  
803 10.5194/acp-17-8553-2017
- 804 Wüst, S., & Bittner, M. (2008, March). Gravity wave reflection: Case study based  
805 on rocket data. *Journal of Atmospheric and Solar-Terrestrial Physics*, *70*(5),  
806 742–755. Retrieved from <https://doi.org/10.1016/j.jastp.2007.10.010>  
807 doi: 10.1016/j.jastp.2007.10.010
- 808 Wüst, S., Bittner, M., Espy, P. J., French, W. J. R., & Mulligan, F. J. (2022, Au-

- 809           gust). Hydroxyl airglow observations for investigating atmospheric dynamics:  
810           results and challenges. *Atmospheric Chemistry and Physics*. Retrieved from  
811           <https://doi.org/10.5194/acp-2022-528> doi: 10.5194/acp-2022-528
- 812       Wüst, S., Bittner, M., Yee, J.-H., Mlynczak, M. G., & III, J. M. R. (2017, Decem-  
813       ber). Variability of the brunt-väisälä frequency at the OH\* layer height. *Atmo-  
814       spheric Measurement Techniques*, *10*(12), 4895–4903. Retrieved from [https://  
815       doi.org/10.5194/amt-10-4895-2017](https://doi.org/10.5194/amt-10-4895-2017) doi: 10.5194/amt-10-4895-2017
- 816       Wüst, S., Wendt, V., Schmidt, C., Lichtenstern, S., Bittner, M., Yee, J.-H., ...  
817       III, J. M. R. (2016, February). Derivation of gravity wave potential energy  
818       density from NDMC measurements. *Journal of Atmospheric and Solar-  
819       Terrestrial Physics*, *138-139*, 32–46. Retrieved from [https://doi.org/  
820       10.1016/j.jastp.2015.12.003](https://doi.org/10.1016/j.jastp.2015.12.003) doi: 10.1016/j.jastp.2015.12.003
- 821       Yoshimura, R., Iwagami, N., & Oyama, K.-I. (2003, September). Rocket mea-  
822       surement of electron density and atomic oxygen density modulated by at-  
823       mospheric gravity waves. *Advances in Space Research*, *32*(5), 837–842. Re-  
824       trieved from [https://doi.org/10.1016/s0273-1177\(03\)00422-8](https://doi.org/10.1016/s0273-1177(03)00422-8) doi:  
825       10.1016/s0273-1177(03)00422-8



**Abstract**

In this study, we apply the three-dimensional Stockwell Transform (3DST) to a novel dataset, namely airglow imager data from Rothera (68°S, 68°W). We use this approach to investigate small-scale high-frequency gravity waves (GWs) in the hydroxyl (OH) airglow layer, at a height  $\sim 87$  km in the mesosphere and lower thermosphere (MLT). MLT GWs are often underrepresented in models, being parameterised due to their small scale size and as such, the significant quantities of momentum and energy transferred by these small waves are missed. Better quantification of these waves is thus required to support future model development. We find that the 3DST can identify waves and extract wave properties and their locations. Horizontal wavelengths are observed ranging from 10 to 40 km and vertical wavelengths of 15 to 40 km, with wave periods of 5 to 9 minutes, peaking at 7.5 minutes. These values are consistent with previous studies. Group speeds are found to be non-zero and large, implying that these GWs travel horizontally and fast. This case study demonstrates that the 3DST can be applied to airglow imager data and can successfully extract GW parameters. This is an important step in automating GW analysis in airglow.

**1 Introduction**

Atmospheric gravity waves (GWs) are fluid-dynamical waves which propagate through the atmosphere and are critical to the dynamics, transport and circulation of the stratosphere, mesosphere and thermosphere (Fritts & Alexander, 2003; Fritts et al., 2006). They are mainly generated in the lower atmosphere by sources including mountains, convective storms, and dynamical systems such as jets, and have spatial scales of ten to hundreds of kilometres and temporal scales from five minutes to several hours.

Due to the decrease of density with height, GWs grow in amplitude as they ascend into the mesosphere and lower thermosphere, eventually overturning, breaking and depositing the energy and momentum they transport from their source into the mean flow. This deposition is sufficiently large to force a meridional flow through zonal drag, driving the mesopause temperature up to 100 K from radiative equilibrium ((Lindzen, 1981; Becker, 2012), and initiating a residual circulation from the cold summer to the warm winter pole. As global circulation models extend upwards into the mesosphere/lower thermosphere (MLT) system and beyond, they must hence be able to reproduce either GWs and/or the energy and momentum they transport accurately. Current models fail to recreate much of the GW activity responsible for controlling and determining the global circulation, as the waves exist at spatial and temporal scales which are not resolved by models of this type. To compensate for this missing effect, the waves are instead parameterised in such models. To do so effectively, the GW parametrisations must be tuned to represent the real atmosphere, accurately depicting the waves' impact on the atmosphere.

Previous observational and modelling studies have found that GW activity is particularly intense in the wintertime over the Southern Andes and the Antarctic Peninsula (Kogure et al., 2021; Hindley et al., 2015; Baumgaertner & McDonald, 2007; Alexander & Teitelbaum, 2007). This region is distinguished by steep topography, high winds over the Southern Ocean, and ferocious frontal activity, which together lead to the generation of strong orographic, convective, and jet-front GWs. As such, knowledge of the behaviour of the waves in the MLT above this region is especially important to guide future model development. This strong GW activity is well-known, and as such a wide range of wave-resolving instruments have been deployed to this region over the past few decades. Consequently, we are now able to investigate these GWs in many ways, such as satellites, rockets, balloons and ground-based techniques (Hindley et al., 2022; Perrett et al., 2021; Hindley et al., 2019; Moffat-Griffin & Colwell, 2017; Wright et al., 2017; Wüst & Bittner, 2008; Goldberg, 2004; Yoshimura et al., 2003).

68 One commonly-used technique for both satellite and ground-based GWs observa-  
 69 tions is to exploit atmospheric airglow. Physically, this airglow is caused by photon emis-  
 70 sions from chemiluminescent processes which involve species such as atomic oxygen, atomic  
 71 nitrogen, and hydroxyl radicals (Khomich et al., 2008). This phenomenon, also known  
 72 as nightglow, acts as a passive tracer for atmospheric dynamics in the MLT, facilitat-  
 73 ing the study of GWs via imagers, rockets and satellites (e.g. Ganaie et al. (2022); Kogure  
 74 et al. (2020); Hu, Ma, Yan, Hindley, Xu, and Jiang (2019a); Miller et al. (2015); Gard-  
 75 ner and Taylor (1998); Takahashi et al. (1996); Taylor et al. (1993); Peterson (1979)).

76 Several energy bands contribute to the total visible and short-wave infrared air-  
 77 glow intensity observed at ground level, but the intensity in the short-wave infrared re-  
 78 gion is substantially higher in hydroxyl (OH) than at other infrared wavelengths. Specif-  
 79 ically, in the short-wave infrared regime lie the Meinel bands, initially studied by Meinel  
 80 (1950), which arise from rotational and vibrational atomic transitions (von Savigny, 2015).  
 81 OH is the primary radiation source of the near-infrared (NIR) airglow layer, which is cen-  
 82 tred at 87 km in height and has a full-width-half-maximum of around 8 km (Baker &  
 83 Stair, 1988), varying in altitude by typically a few kilometres (von Savigny, 2015; Wüst  
 84 et al., 2016, 2022).

85 GWs appear in airglow layers as a result of changes in pressure and temperature  
 86 caused by the waves passing through the medium, which lead to intensity fluctuations  
 87 in the observed emitted radiation. Many previous studies have shown that OH airglow  
 88 emissions are excellent tracers for observing atmospheric properties and studying dynam-  
 89 ical processes such as instabilities, ripples, small-scale GWs, and larger-scale atmospheric  
 90 waves such as tides and planetary waves (Sedlak et al., 2020; J. Li et al., 2017; Cao &  
 91 Liu, 2016). The spectral properties of small-scale GWs in the MLT, such as wavelengths,  
 92 phase speeds, and propagation directions, can hence be directly observed in the airglow  
 93 layers by using optical imagers. Previous studies have observed GWs with typical hor-  
 94 izontal wavelengths of 20-100 km, intrinsic wave periods of 5 – 10 minutes, and horizon-  
 95 tal phase speeds ranging from 30 to 100  $\text{ms}^{-1}$  (Ejiri et al., 2003; Taylor et al., 1997; Z. Li  
 96 et al., 2011). These limits are imposed by the spatial extent airglow imagers can observe  
 97 and the cadence of images taken.

98 In this study, we present a novel application of the three-dimensional Stockwell Trans-  
 99 form (S-Transform) to OH airglow imager data from the British Antarctic Survey base  
 100 at Rothera (68°S, 68°W), using data from the night of the 26th – 27th April 2012 as both  
 101 as a case study and a demonstration of the technique. We use the S-Transform to ob-  
 102 serve wave parameters (i.e. wavelengths and periods) and then calculate meteor radar  
 103 winds from the same location to compensate for the Doppler-shifting effects of the wind  
 104 and establish ‘intrinsic’ wave parameters, i.e. in the frame of reference of the wave.

105 In Section 2 we describe the data sources, firstly from the airglow imager and sec-  
 106 ondly from the meteor radar. Section 3 deals, firstly, with the airglow image processing,  
 107 secondly with the S-Transform analysis, thirdly with the meteor radar winds and finally  
 108 with the calculation of wave parameters. Section 5 discusses our method and results in  
 109 the context of previous studies. Finally, in Section 6 we provide our conclusions and a  
 110 future outlook on how this semi-automated method could be applied more broadly.

## 111 2 Data

### 112 2.1 Airglow Imager

113 Airglow imagers have an extensive track record as a tool for detecting and char-  
 114 acterising GWs in atmospheric airglow layers (e.g. Nielsen et al. (2009); Matsuda et al.  
 115 (2014); Rourke et al. (2017)). Here, we use an all-sky (180°) monochromatic filter imag-  
 116 ing system to observe GWs in the  $\sim 87$  km OH airglow layer. The specific instrument used  
 117 measures these OH signals with a 15-second exposure period, and also measures weaker

118 O<sub>2</sub> and Na signals at 90-second and 120-second exposure periods respectively. Combined,  
 119 this gives an overall measurement cadence of  $\sim 6$  min with an embedded 2-minute OH  
 120 cadence. Figure 1 illustrates the approximate emission distribution of these layers as a  
 121 function of height; we use only the OH data here as proof-of-concept, but future stud-  
 122 ies could exploit these additional layers to provide 4D (i.e. distance/height/time) GW  
 123 information from the same site. Similar systems have been used in past studies to anal-  
 124 yse short-period GWs (e.g. Taylor et al. (1997); Pautet (2005); Nielsen et al. (2006))

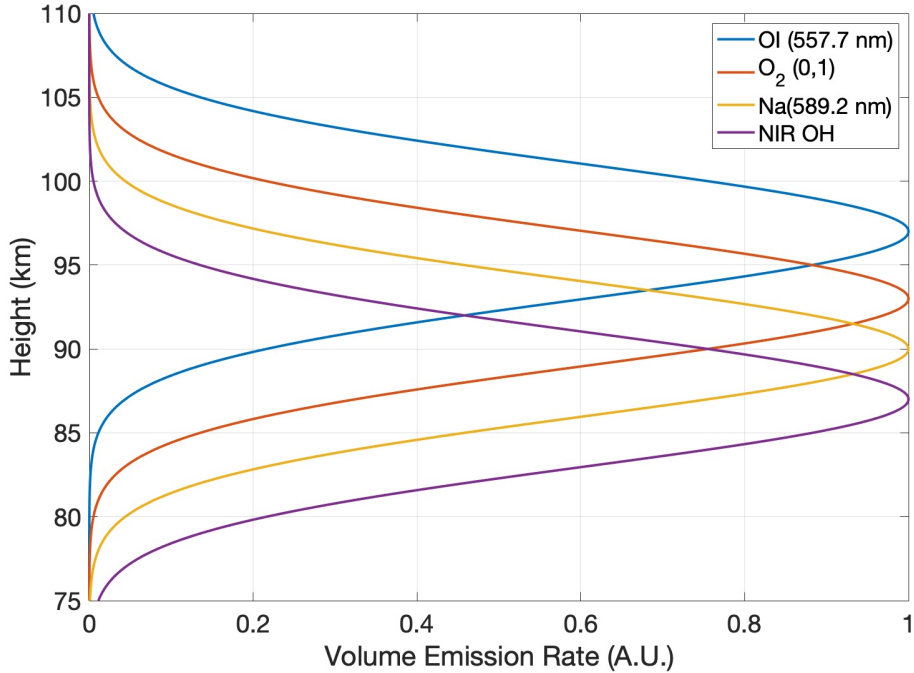


**Figure 1.** Diagrammatic representation of the heights and volume emission rate of four MLT airglow species. Adapted from Nielsen (2007).

## 125 2.2 Meteor Radar

126 Meteor radars are a well-established means of monitoring MLT winds at heights  
 127 from 75 to 105 km. As such, they have been widely used for ground-based tidal and GW  
 128 studies (e.g. Hindley et al. (2022); Stober et al. (2021); Dempsey et al. (2021); Davis et  
 129 al. (2013); Beldon et al. (2006); Mitchell (2002)).

130 Here, we use a SKYiMET meteor radar located at the British Antarctic Survey base  
 131 at Rothera (68°S, 68°W).

132 This instrument was deployed in 2005 and has been operating almost continuously  
 133 from 2005 up to the present. Hocking et al. (2001) provide a full explanation of the SKiYMET  
 134 radar operation.

135 We calculate horizontal winds from raw meteor measurements according to the method  
 136 outlined by Hindley et al. (2022), combining the inferred individual horizontal veloci-  
 137 ties for each meteor using a Gaussian weighting in height and time around a specified  
 138 height and time. These Gaussian weightings have full-width-half-maxima of 2 hours in  
 139 time and 3 km in height. We move the centre of each Gaussian over the data in 1 hour

140 time and 1 km height steps, yielding winds at an hourly resolution across the height range  
 141 from 75 to 105 km. This approach has previously been applied by both Dempsey et al.  
 142 (2021) and Hindley et al. (2022). We use these inferred winds to convert our GW mea-  
 143 surements from the ground-based to the intrinsic frame of reference, linearly interpolat-  
 144 ing the winds to the time of each airglow image to provide local zonal and meridional  
 145 wind estimates.

### 146 3 Method

147 Our S-Transform GW analysis, described below, is based on a Fourier Transform  
 148 algorithm and thus requires the input data to be regularly-gridded in both space and time.  
 149 We also need to remove fast- and slowly-varying background features. Accordingly, the  
 150 data require some preprocessing before they can be analysed. Figure 2 presents the steps  
 151 in our airglow image preprocessing and processing chain. The units of the data are ar-  
 152 bitrary brightness units recorded by the imager, but are consistent between panels.

153 Figure 2a shows an example raw image obtained from the instrument. GWs are  
 154 visually apparent in the frame as curved striped features, but are overlaid by consider-  
 155 able noise from stars and from the Milky Way Galaxy, which in this frame runs through  
 156 the middle of the image. In addition, as there is no geographic metadata stored by the  
 157 imager other than the time of each frame, we need to produce this geographic informa-  
 158 tion.

159 Therefore, we must first convert the observed pixel positions to a spatial location  
 160 (i.e. latitude and longitude) and also remove the stars and the galaxy. The galaxy re-  
 161 moval step is particularly important in this regard: as it is a bright rotating near-linear  
 162 object, application of spectral analysis techniques are likely to identify its rotation as the  
 163 wave to be studied, rather than the overlying small amplitude ripples and bands which  
 164 are the our target.

#### 165 3.1 Airglow Imager Geometry

166 We first convert coordinate frames, with the aim of geolocation each pixel in the  
 167 raw data to a specific spatial distance and direction from the centre of rotation of the  
 168 image, i.e. the vertical axis above the imager. For this purpose, we assume (i) that the  
 169 airglow layer we are observing is at 87 km, (ii) that the zenith, i.e. directly above the Rothera  
 170 airglow imager, is in the middle of the frame and (iii) that the edge of the frame repre-  
 171 sents the horizontal plane of the ground. Using the angle subtended by each pixel from  
 172 the centre pixel, we can then geometrically calculate the latitude and longitude, or ra-  
 173 dius and direction, of each point in the frame.

174 Figure 3 presents the geometry of the airglow layer used to compute this conver-  
 175 sion. To do this, we calculate the arc length,  $a$ , from the zenith position. Under the as-  
 176 sumption that the airglow layer is at a height  $h$  of 87 km above the observer at  $P$ , each  
 177 pixel location  $Q$  makes a right-angled triangle with angle  $\theta$  subtended. This angle allows  
 178 us to calculate the arc length,  $a$ , of the point  $Q$ .  $R_E$  is the radius of the Earth and  $r =$   
 179  $R_E + h$ .

180 The first step is to calculate the location of  $P$  in the PQ plane,  $P^+$ . This is given  
 181 by:

$$P^+ = (P_x^+, P_y^+) = (R_E \cos \theta, R_E \sin \theta) \quad (1)$$

182 We may use this to calculate the angle  $\beta$  as:

$$\beta = \phi - \alpha \quad (2)$$

## Airglow Imager Data Processing

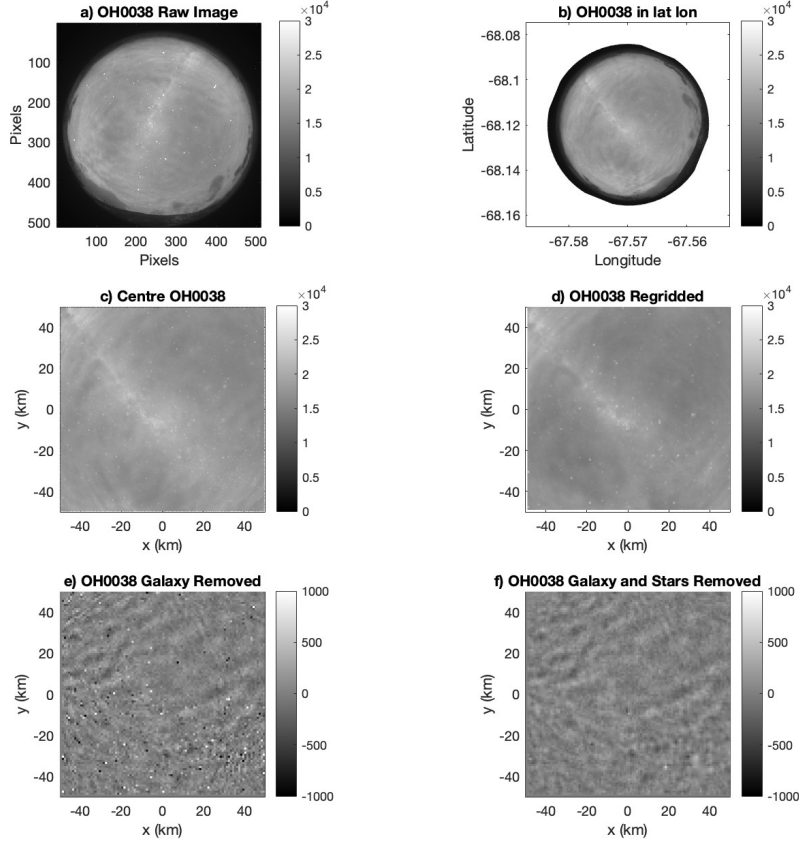


**Figure 2.** Processing steps of the airglow images explained for one image. Panel a) presents the raw image as given in the tif file, b) presents the image projected on a latitude/longitude grid, c) is the centre 100 km square around the zenith, d) is the centre 100 km around the zenith interpolated onto a regularly spaced grid, e) is the centre grid following the FFT galaxy removal and finally f) presents the field of view with a final step of star removal performed.

$$\tan\alpha = \frac{P_x^+}{P_y^+} \quad (3)$$

$$\cos\phi = \frac{P_y^+}{r} \quad (4)$$

183

This means that:

$$\beta = \cos^{-1}\left(\frac{P_y^+}{r}\right) - \tan^{-1}\left(\frac{P_x^+}{P_y^+}\right) \quad (5)$$

$$\beta = \cos^{-1}\left(\frac{R_E \sin\theta}{r}\right) - \tan^{-1}\left(\frac{R_E \cos\theta}{R_E \sin\theta}\right) \quad (6)$$

184

The arc length is therefore given by:



203 pixels. Only pixels exceeding a cutoff of the 98th percentile are dealt with this way, and  
 204 this does leave some stellar signatures which we address below. We can see that we have  
 205 not lost any geophysical information concerning the airglow layer in this step, and the  
 206 waves present in the original image can still be seen.

207 We now move onto the dominant background feature of the Milky Way galaxy. This  
 208 is one of the most visually noticeable features of the sky, especially in dark locations such  
 209 as Rothera. To remove this signal do this, we perform a three-dimensional FFT on the  
 210 image and then remove low temporal frequencies, i.e. signals with long and regular tem-  
 211 poral periods. This is done using a 3D Fast Fourier Transform, the inverse FFT returns  
 212 Figure 2e, in which the signature of the galaxy has been very significantly ameliorated.  
 213 The stars, however, are still present in the frame and could be identified by the S-Transform  
 214 as strong waves with very short periods and wavelengths. The final step, therefore, is  
 215 to more strongly remove the stars. We do this using a difference filter, where we com-  
 216 pute the difference between adjacent pixels time, i.e. between frames. Specifically, we  
 217 identify those pixels which show a difference of over 300 (in arbitrary units) between frames  
 218 and remove the value, replacing it with the mean of the surrounding values. This returns  
 219 Figure 2f where the processed data appears with no strong signatures of either stars or  
 220 the galaxy and with the target waves now very visually prominent.

### 221 3.2 S-transform Wave Analysis

222 When extracting wave properties from airglow data, a conventional Fourier trans-  
 223 form analysis can identify the frequencies present in the data; however, it cannot iden-  
 224 tify where and when these frequencies occur in geospatial coordinates. For this, another  
 225 method is required. Accordingly, in this study we apply the 3-D Stockwell transform (3DST)  
 226 technique described by Wright et al. (2017) and Hindley et al. (2019) to measure the spec-  
 227 tral properties of GWs, using two dimensions of space (northwards and eastwards) and  
 228 one of time. Based upon the work of R. Stockwell et al. (1996) and Hindley et al. (2016),  
 229 this method provides a voxel-by-voxel estimate of the amplitude, spatial and temporal  
 230 frequency and direction of propagation of the strongest wavelike signal at every location  
 231 in the 3-D (i.e.  $x$ ,  $y$ ,  $t$ ) data volume. From these estimated properties, we are further able  
 232 to infer properties such as phase speed and vertical wavelength, as described below.

233 The S-transform has been extensively used in previous GW studies (R. G. Stock-  
 234 well & Lowe, 2001; McDonald, 2012; Wright & Gille, 2013; Hindley et al., 2016; Hu, Ma,  
 235 Yan, Hindley, Xu, & Jiang, 2019b; Hu, Ma, Yan, Hindley, & Zhao, 2019; Hindley et al.,  
 236 2019), and demonstrated to be a highly capable technique for measuring and localising  
 237 frequencies (or wavenumbers) and their associated amplitudes. However, these previous  
 238 gravity wave studies have used it in spatial dimensions only, and applying it to mixed  
 239 space/time data as we do here is a novel approach. By limiting the range of permitted  
 240 frequencies over which the spectral windows are applied, we are also in principle able to  
 241 select for different periods and wavelengths to allow the investigation of ripples and bands;  
 242 however, as this study is a demonstration of the method, we have not, in this case, re-  
 243 stricted the frequencies detected in this way.

### 244 3.3 Calculating Wave Properties

245 With the measured parameters from the S-Transform, supported by wind data from  
 246 the meteor radar, we can calculate both observed and intrinsic wave parameters, i.e. the  
 247 wave parameters in both ground-based Eulerian and wind-following Lagrangian frames  
 248 of reference.

249 To do this, we first use the 3DST to measure the horizontal wavenumbers ( $k$  and  
 250  $l$  in the zonal and meridional directions, respectively), period, frequencies, wavelengths  
 251 and amplitudes of the observed waves. From these, we can directly compute the hori-

252 zontal wave phase speed  $c_p$  as  $c_p = \omega/k_h$ , where  $\omega$  is the measured angular frequency  
 253 and  $k_h$  is the Pythagorean sum of  $k$  and  $l$ . We can then calculate the intrinsic frequency,  
 254  $\hat{\omega}$ , given by

$$\hat{\omega} = \omega - k\bar{u} - l\bar{v} \quad (9)$$

255 where  $\bar{u}$  is the background zonal wind and  $\bar{v}$  is the background meridional wind. To do  
 256 this, we use hourly wind values from the radar data linearly interpolated to each image  
 257 time.

258 The intrinsic horizontal phase speed,  $\hat{c}_p$ , can then be computed as  $\hat{c}_p = c_p - \bar{u}_h$   
 259 where  $\bar{u}_h$  is the Pythagorean sum of  $u$  and  $v$ . Using the medium frequency GW approx-  
 260 imation (Fritts & Alexander, 2003), such that the absolute value of vertical wavenum-  
 261 ber,  $m$ , is given by  $|m| = N/|\hat{c}_p|$  where  $N$  is the Brunt-Väisälä frequency and  $\hat{c}_h$  is the  
 262 intrinsic horizontal phase speed, this allows us to calculate  $\lambda_z = 1/m$ .

263 We can then calculate the intrinsic frequency:

$$\hat{\omega} = N \left| \frac{k_h}{m} \right| \quad (10)$$

264 and also the intrinsic group speed  $\hat{c}_g$ :

$$\hat{c}_g = \bar{u} + \frac{\hat{\omega}}{k_h} \quad (11)$$

265 Once we have performed these calculations we have the following parameters:

- 266 • horizontal and vertical wavelengths,  $\lambda_h$  and  $\lambda_z$ , respectively
- 267 • observed and intrinsic frequencies,  $\omega$  and  $\hat{\omega}$ , respectively
- 268 • observed and intrinsic horizontal phase speeds,  $c_p$  and  $\hat{c}_p$ , respectively
- 269 • observed and intrinsic group speeds,  $c_g$  and  $\hat{c}_g$ , respectively
- 270 • direction
- 271 • and finally period  $T$ .

## 272 4 Results

### 273 4.1 Initial Visual Analysis

274 Figure 4 presents a time series of waves above an S-Transform-derived amplitude  
 275 threshold over the time period 23:35 to 01:05 on the night of the 26th – 27th of April  
 276 2012.

277 In this figure, to highlight only the strongest wave features results are only shown  
 278 where the S-Transform output amplitude is above a cutoff value of 200 units, illustrated  
 279 by a faint semitransparent grey wrapper. This cutoff represents a value close to the 90th  
 280 percentile of the full measured amplitude distribution including noise-dominated regions.  
 281 Within this volume, red and blue isosurfaces represent phase fronts of positive and neg-  
 282 ative perturbations from the background state as the wave moves across the imager’s field  
 283 of view; the outer (semi-transparent) red and blue surfaces enclose values greater than  
 284 10 units and the solid inner surfaces values greater than 45 units.

285 The blue and red isosurfaces can then be interpreted as a visual depiction of the  
 286 wave’s phase fronts as they advance through time. Distinct wavefronts can be seen through-  
 287 out the chosen period, with the region falling within the amplitude cutoff envelope grad-  
 288 ually increasing as the wave covers a larger fraction of the total observed area. We also

289 see two instances of other waves growing and then dissipating separately to the main wave  
 290 envelope. We thus conclude that these waves are indeed persistent and large enough to  
 291 proceed with our investigation.

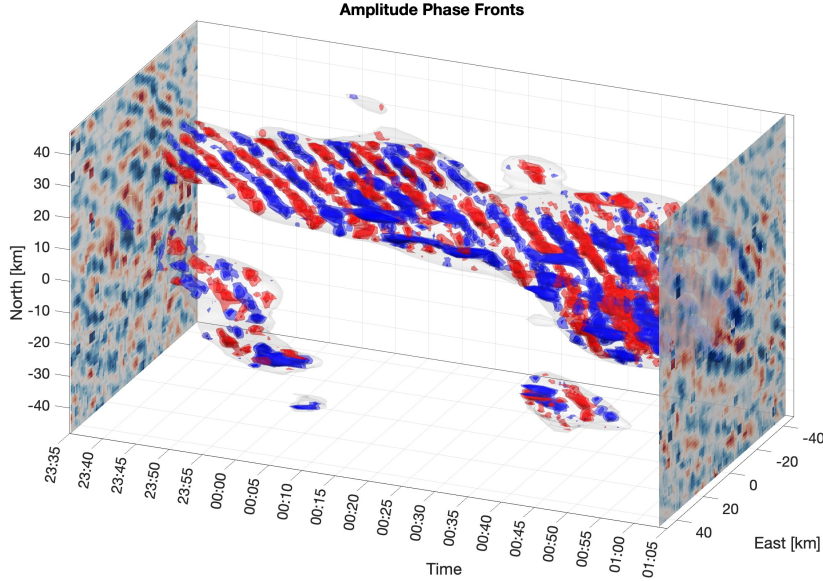


**Figure 4.** 3D visualisation of wave phase fronts over the time period 23:25 to 01:05 on the night of the 26th – 27th April. Here we have selected waves based on an amplitude threshold. This wave envelope is given in light grey shading around the wave packets. The wave is persistent across the time period and the area of influence increases.

292 **4.2 S-Transform Analysis - Example Results**

293 As described above, from the S-Transform we are able to extract wave amplitude,  
 294 horizontal wavelengths, frequency and period of each pixel in an image. This allows us  
 295 to build a picture of the waves and their properties as they vary over time.

296 Figure 5 presents an example of a single frame from the output of the 3D S-Transform  
 297 as applied to the airglow imager data over the night of the 26th – 27th April 2012. Fig-  
 298 ure 5a shows the input data, b the reconstructed wave field based on the output, c the  
 299 wave amplitude at each point on the image, d the horizontal wavelength calculated as  
 300 a Pythagorean sum of the wavelengths in the x and y directions, e the direction of prop-  
 301 agation and f the period in minutes. It can be seen from this example that the wave seen  
 302 in the input data and our above time-varying example is clearly detected by the anal-  
 303 ysis.

304 In Figure 5a, we can visually identify wave fronts in the image, which are clear to  
 305 the eye and free from major interference. This means that they are well-placed to be re-  
 306 covered by the S-Transform. A similar picture is seen in Figure 5b, where we reconstruct  
 307 the detected wave field reconstruction (as described by Hindley et al. (2016)). As this  
 308 field is visually and quantitatively similar to the input, we can be confident that the wave  
 309 properties we are calculating using the S-Transform are reliable. In Figure 5c we then  
 310 show the amplitude calculated for each pixel on the image. We see that the area with  
 311 more pronounced wave features marked with a black box in Figure 5a – d in the input  
 312 data exhibits stronger amplitudes than signals in the rest of the figure.

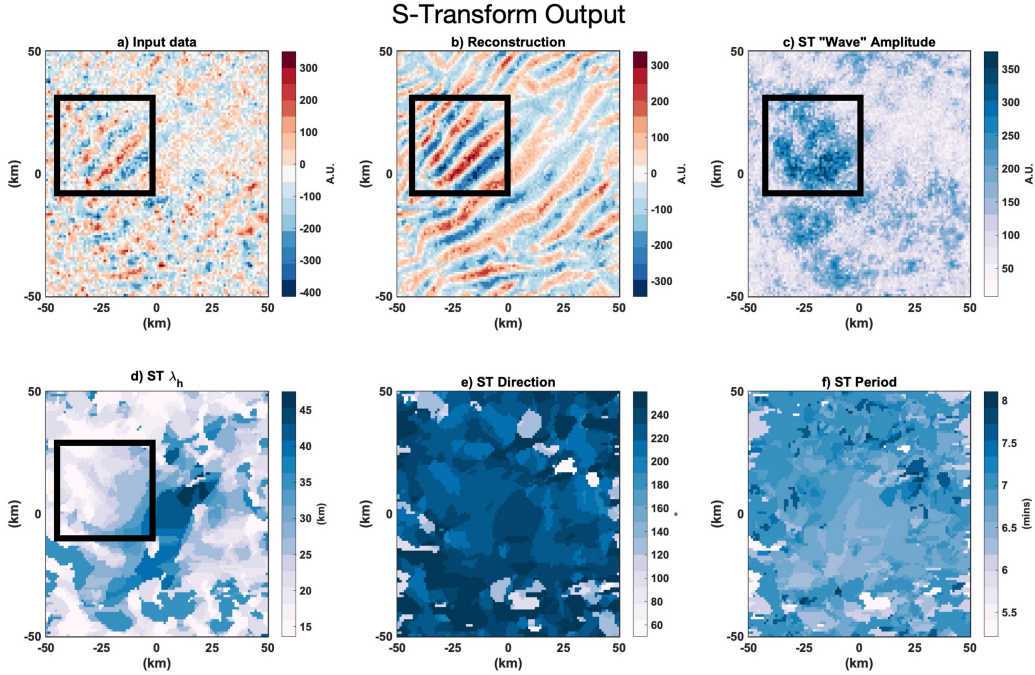


**Figure 5.** Examples of the S-Transform output. In panel a, the input data following the star and galaxy removal, b presents the reconstruction of the wave field given the wave properties, c shows the amplitude of the wave at each pixel, d presents the horizontal wavelength as a Pythagorean sum of the x and y directions, e direction propagation of the dominant wave at each pixel and f presents the period in minutes.

313 Further, we show the wavelength in the horizontal direction in Figure 5d. A brief  
 314 visual check shows that the long wavelengths present in the input data are picked  
 315 up by the S-Transform in the reconstruction and in this field. Finally, the periods are  
 316 shown in Figure 5f ranging from around 5 to 8 minutes. These are fast waves, as the Brunt-  
 317 Väisälä period at this height is around 5 minutes (Wüst et al., 2017).

### 318 4.3 S-Transform Analysis - All-Night Results

319 We now show integrated results over the entire night. Figure 6 presents histograms  
 320 of this output, as quantified at the voxel level. Specifically, we have defined this dataset  
 321 such that each voxel above the 90th percentile threshold used previously for Figure 4 con-  
 322 tributes a single count to each histogram. The histograms are defined across 15 equally-  
 323 sized bins, with the bin width calculated by computing the range between the maximum  
 324 and minimum values and dividing this range into 15 equal-width bins. Here we present  
 325 the horizontal wavelength  $\lambda_h$  in Figure 6a, the vertical wavelength  $\lambda_z$  in b, the angular  
 326 frequency  $\omega$  in c, the phase speed  $c_p$  in d, the group speed  $c_g$  in e, the direction in f, the  
 327 temporal period  $T$  in g, the intrinsic angular frequency  $\hat{\omega}$  in h, the intrinsic phase speed  
 328  $\hat{c}_p$  in i, and the intrinsic group speed  $\hat{c}_g$  in j.

329 The distribution of horizontal wavelengths seen in Figure 6a shows that measured  
 330 horizontal wavelengths are generally below 30 km. However, there is also a distinct peak  
 331 at wavelengths  $\sim 35$  km. This peak likely arises due to the histograms being computed  
 332 from voxel-level rather than wave-level data: such a feature is consistent with a promi-

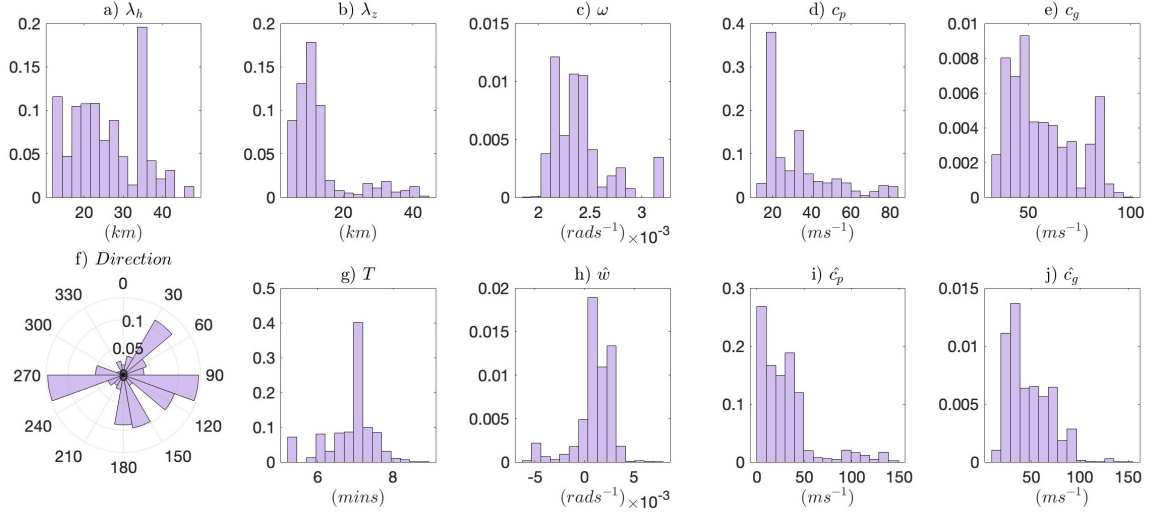


**Figure 6.** Histograms of the wave properties extracted from the airglow images using the 3D S-Transform for the night of 26th – 27th April 2012. Presented here are the horizontal wavelength  $\lambda_h$  in a), the vertical wavelength  $\lambda_z$  in b), the angular frequency  $\omega$  in c), the phase speed  $c_p$  in d), the group speed  $c_g$  in e), the direction in f), the temporal period  $T$  in g), the intrinsic angular frequency  $\hat{\omega}$  in h), the intrinsic phase speed  $\hat{c}_p$  in i), and the intrinsic group speed  $\hat{c}_g$  in j).

333      nent and persistent wave that lasts for multiple frames contributed a large number of counts  
 334      in this bin. If we had a method that counted a wave only once as it progressed over the  
 335      image, we would expect this peak to be less pronounced. However, defining the limits  
 336      of a wave packet within data of this type is a non-trivial exercise and developing a method  
 337      such as this is beyond the scope of this paper.

338      Vertical wavelengths in Figure 6b shows smaller wavelengths below 20 km are more  
 339      common than those above 20 km. We can see the peak of this distribution is around 16  
 340      km.

341      The angular frequencies computed for the waves, shown in Figure 6c, suggest a pref-  
 342      erence for values below  $2.5 \text{ rad s}^{-1}$ , but with a noticeable secondary peak apparent at  
 343      values  $\sim 3.1 \text{ rad s}^{-1}$ . In Figure 6d the phase speeds show a preference for lower speeds  
 344      with a peak at  $20 \text{ ms}^{-1}$  and at  $35 \text{ ms}^{-1}$ . We can see phase speeds of 15 to  $90 \text{ ms}^{-1}$ . Larger  
 345      speeds are, however, less common. The group speed in Figure 6e shows presents two peaks,  
 346      one at  $55 \text{ ms}^{-1}$  and one at  $90 \text{ ms}^{-1}$ . Group speeds between  $25 \text{ ms}^{-1}$  and  $75 \text{ ms}^{-1}$  are  
 347      more common than speeds between  $75 \text{ ms}^{-1}$  and  $100 \text{ ms}^{-1}$ , but both are still prominent.

348      Figure 6f presents the direction of the waves displayed as a bearing (clockwise from  
 349      north). We can see that some directions are more prominent, i.e. northeast, east-southeast  
 350      and west-southwest. There are also some waves travelling south.

351      We present the periods of the waves in Figure 6g where the most common period  
 352      is at 7 minutes, with periods from 5.5 mins to 8 mins also being present. Above 8 mins,  
 353      there are limited instances of waves present.

354      The following parameters are intrinsic wave parameters; that is, they are the wave  
 355      parameters from the frame of reference of the wind the wave propagates through. In Fig-  
 356      ure 6h, presenting intrinsic angular frequency, we can see an almost symmetrical distri-

357 bution surrounding  $0 \text{ rad s}^{-1}$  implying that in the wave frame of reference, waves are  
 358 travelling both with and against the wind. In Figure 6i, we present the intrinsic phase  
 359 speed where a preference for lower speeds is evident, specifically below  $50 \text{ ms}^{-1}$ . Speeds  
 360 between  $100 \text{ ms}^{-1}$  and  $150 \text{ ms}^{-1}$  are observed, but this is a very low occurrence. Finally,  
 361 intrinsic group speed shows an almost log-normal distribution with speeds between  $10$   
 362  $\text{ms}^{-1}$  and  $130 \text{ ms}^{-1}$  with a peak at around  $25 \text{ ms}^{-1}$ .

363 In Figure 6e, we observe group speeds which are large and non-zero. This implies  
 364 that the waves we see are not only travelling fast but horizontally propagating. This is  
 365 at odds with common GW parameterisations which consider GWs as being constrained  
 366 to the vertical column of a single gridbox and which can only propagate vertically within  
 367 this column (Alexander et al., 2010; Kalisch et al., 2014). These results provide further  
 368 evidence that this is not the case and that GW parameterisations which do not consider  
 369 horizontal propagation are unsuitable for capturing these small-scale waves which carry  
 370 significant quantities of energy and momentum (Geller et al., 2013; Alexander et al., 2010).

## 371 5 Discussion

372 Since in our study we apply a novel method, it is important to assess our results  
 373 properly in the context of previous work using more conventional approaches. Accord-  
 374 ingly, in this section we compare our results quantitatively to previous studies (section  
 375 5.1), before discussing the advantages and disadvantages of our approach relative to other  
 376 available methods (section 5.2).

### 377 5.1 Results Comparison to Previous Studies

378 We have found horizontal wavelengths ranging from around 5 to 45 km, with most  
 379 voxels being associated with values between 20 – 25 km. This compares favourably with  
 380 previous studies, which show wavelengths between 20 – 30 km (Kam et al., 2017; Pautet,  
 381 2005; Ejiri et al., 2003; Hecht et al., 2001; R. Stockwell et al., 1996), and with peaks at  
 382 35 km seen in (Hecht, 2002).

383 Nielsen et al. (2009) investigated GWs in the hydroxyl airglow layer, using data  
 384 from when the same imaging system used in our study was deployed instead to the British  
 385 Antarctic Survey base at Halley, Antarctica ( $76^\circ\text{S}$ ,  $27^\circ\text{W}$ ). They investigated the sea-  
 386 sonal climatology of individual quasi-monochromatic, short-period gravity-wave char-  
 387 acteristics at high-southern latitudes. These characteristics were observed over the 2000  
 388 and 2001 austral winter seasons. They found horizontal wavelengths from 10 – 70 km,  
 389 producing a log-normal distribution with a peak at 15 – 20 km. Comparatively, we have  
 390 observed a range of 10 – 50 km with a high count at 35 km. As we test only a single night  
 391 of data, this difference may simply be due to the most dominant wave on this specific  
 392 night having this wavelength. As the S-Transform gives us voxel-level information, not  
 393 individual wave events, we cannot say how many waves had this wavelength with this  
 394 information alone.

395 Similarly, for observed wave periods, we see a range of values from 5 – 9  $\text{ms}^{-1}$  with  
 396 a peak at around  $7.5 \text{ ms}^{-1}$ . Nielsen et al. (2009) found a range of 5 – 30  $\text{ms}^{-1}$  with a  
 397 log-normal distribution with peak at  $\sim 7.5 \text{ ms}^{-1}$ . This is broadly similar to the peak we  
 398 have seen, which suggests that this is a common wave period. The wide range of peri-  
 399 ods seen in their study will come from the two winters of data that have been used. We  
 400 have used one night to benchmark our method resulting, therefore, in less data and fewer  
 401 wave events.

402 The directions observed by Nielsen et al. (2009) showed a clear preference for prop-  
 403 agation towards the South Pole, and there is limited evidence of waves propagating North.

404 Similarly, we have shown that propagation southwards is apparent in our case; however,  
405 the directions we observed also peak significantly in the WSW and ESE directions.

406 Kam et al. (2017) observed a very similar range of observed phase speeds as in our  
407 study; however, the periods we observe are faster, with a range from 5 – 9 minutes com-  
408 pared with the range of 5 – 60 minutes in the work of Kam et al. (2017). This also sug-  
409 gests that the results we have uncovered using the 3DST are plausible.

410 With observed phase speed, Nielsen et al. (2009) saw a range from 0 to 100  $\text{ms}^{-1}$   
411 with a peak at 30 to 40  $\text{ms}^{-1}$ . This is an almost Gaussian distribution. We observe a  
412 range from 10 to 90  $\text{ms}^{-1}$ , very similar to that observed at Halley. We also observed a  
413 peak at 20  $\text{ms}^{-1}$ . This could be a persistent wave event that was spatially large and there-  
414 fore could be present over many voxels.

## 415 5.2 Methodological Comparisons

416 The addition of supporting meteor radar data also allows us to convert these pa-  
417 rameters from the ground-based to the intrinsic frame.

### 418 5.2.1 The 2D Stockwell Transform

419 Here, we apply the 3D Stockwell Transform to data of this type for the first time.  
420 The simpler two-dimensional S-Transform (2DST) has however previously been applied  
421 to airglow data. Specifically, R. G. Stockwell and Lowe (2001) applied the 2DST to 16  
422 x 16 pixel airglow images, covering a field of view of 1.5 km at the height of the airglow  
423 at 87 km. In addition to accounting for time variation, advances in computing power also  
424 allow us to work at a much larger scale, allowing us to apply the technique to a full night  
425 of observations totalling 360 frames, each of 101 by 101 pixels and hence covering an area  
426 of sky equivalent to 100 by 100 km on the surface.

427 This combination of features allows us to quantify wave parameters over a much  
428 larger field of view than (R. G. Stockwell & Lowe, 2001), and to measure many additional  
429 parameters. In particular, the ability to simultaneously obtain both spatial information  
430 and the temporal frequency of these waves and how they covary is a key advantage over  
431 this older 2D approach.

### 432 5.2.2 The Fast Fourier Transform

433 An alternative approach is to use just a 3D FFT without the additional window-  
434 ing properties of the ST. This is computationally very significantly cheaper. As an ex-  
435 ample of this approach, Rourke et al. (2017) investigated short-period GWs and ripples  
436 at Davis Station, Antarctica (68 °S, 78 °E) using a scanning radiometer to measure hy-  
437 droxyl airglow perturbations.

438 The approach of Rourke et al. (2017) identified the dominant wave feature in each  
439 frame using the FFT, with the period of the dominant wave determined from time-variations  
440 in the FFTs of the weighted centre of 32 successive images centred on the frame in ques-  
441 tion. Using a sampling rate of 1 min and a maximum window length of 32, the range  
442 of wave periods detectable by this approach was 2 to 16 minutes. They then used lag  
443 analysis to determine the wave direction and speed.

444 Our method provides similar outputs, but whereas their approach gave results at  
445 the frame level our 3DST approach allows the measurement of geographically-decomposed  
446 parameters at the single-voxel level. This allows for more information to be extracted  
447 about the waves, and for multiple waves in the same panel to be measured.

448

### 5.2.3 Cospectral Analysis

449

450

451

Another method of extracting wave properties is co-spectral analysis, as applied by e.g. Cao and Liu (2022) to airglow images observed at Andes Lidar Observatory (30.3 °S, 70.7 °W) in northern Chile.

452

453

454

455

456

457

458

459

460

In this study, images were unwrapped to a flat field to account for the van Rhijn effect. They removed the galaxy using the Principal Component Analysis (PCA) method from Z. Li et al. (2014), then used three consecutive images to create two time-differenced images. Horizontal wave properties such as wavelength, observed phase speed, direction and relative emission perturbation amplitude were then derived from the co-spectra of the two images, supported as in our study by background winds from a SKiYMET meteor radar system based at the Andes Lidar Observatory to convert between the intrinsic and ground-based frames. Once this step was performed, any wavelengths below 10 km and any periods below the buoyancy frequency were removed.

461

462

463

464

465

466

This method, similar to our 3DST, allowed both observed and intrinsic parameters can be established along with relative emission amplitudes of consecutive images. However, the method also results in some lost information due to taking the direct differences between each frame. Furthermore, it also assumes that the phase difference from voxel to voxel in time is accurate; therefore, any noise present (very likely in real observations) will impact significantly and directly upon the quality of the final results.

467

### 5.2.4 The M-Transform

468

469

470

The final method we discuss is the M-Transform. This was formulated by Matsuda et al. (2014) as a 3D method to extract wave properties, similar in underlying conception to the S-Transform.

471

472

473

474

475

476

477

As with the S-Transform, the M-Transform requires a time series of airglow images with fixed and consistent pixel time spacing. For this method, once again, the airglow images must be preprocessed to remove stars, the galaxy, and any lens effects, and must also be projected onto geographic coordinates. Once this has been done, the M-transform transforms the Power Spectral Density (PSD) in the wavenumber domain ( $k, l, \omega$ ), where  $k$  and  $l$  are the wavenumbers in the zonal and meridional direction, respectively and  $\omega$  is the frequency in the phase velocity domain ( $v_x, v_y, \omega$ ) via the following equations:

$$v_x = \frac{\omega k}{k^2 + l^2} \quad (12)$$

$$v_y = \frac{\omega l}{k^2 + l^2} \quad (13)$$

478

479

Where  $v_x$  and  $v_y$  are the orthogonal projections of the phase velocity onto zonal and meridional axes, respectively. This allows for the calculation of phase speed and azimuth as:

$$(v_x, v_y) = c(\sin\phi, \cos\phi) \quad (14)$$

480

481

Where  $c$  is the phase speed, and  $\phi$  is the azimuth. Finally, the phase velocity is integrated to give a 2D phase velocity spectrum.

482

483

484

485

486

487

488

The M-transform shares many benefits with the S-Transform method we present in this study. For instance, it is highly automated and does not require interaction with the user, it is 3D, and it provides many wave properties directly. However, the M-transform is statistical, and there is no information provided from the analysis about specific locations and times within the dataset used - all properties are measured at the bulk level for the whole dataset. The ability of the S-Transform approach to resolve the same properties at the voxel level is thus a significant advantage.

## 6 Conclusions

In this study, we have presented a new application of a 3D spectral analysis technique, the 3D S-Transform, to airglow imager data from the Antarctic Peninsula at the British Antarctic Survey Base at Rothera (68°S, 68°W).

The method is automated and can identify wave properties for each pixel; we can, therefore, use it to investigate the spatial extent of the wave, as in Figure 4.

We have found that:

1. The 3D S-Transform method works well with processed airglow imager data and measures wave parameters consistent with the airglow literature
2. The majority of waves seen in the airglow in this case study are small, fast GWs with short periods.
3. We see a distribution of horizontal wavelengths between 10 to 50 km with a sharp peak at 35 km, possibly due to methodological reasons
4. Vertical wavelengths peak at values below 20 km, peaking at around 15 km but with the largest peak at around 40 km.
5. Phase speeds are generally low, and group speeds are high and non-zero This suggests that the waves observed are travelling horizontally and also fast, further suggesting that GW parametrisations which do not account for horizontal movement are inadequate
6. Finally, we can give accurate locations of where the waves in the airglow are present due to the 3D S-Transform investigating waves on the pixel rather than wave event level.

Future studies could advantageously use the S-Transform in tandem with an automated image processing technique to improve the process thus allowing the identification of airglow images that are of sufficient clarity for use in the investigation of GWs. Used together, these processes would allow airglow images to be processed and analysed in one programme with little input from the user, allowing for a fully automated process. This would result in GW parameters and their locations on each frame. More work on the spatial extent of the wave could then be performed and investigated.

## Data Availability

The meteor radar data used in this study are archived as part of from Mitchell, N. (2019): University of Bath: Rothera Skymet Meteor Radar data (2005 – present). Centre for Environmental Data Analysis, 2022. <https://catalogue.ceda.ac.uk/uuid/aa44e02718fd4ba49cefe36d884c6e>

## Acknowledgments

SMD is supported by a NERC GW4+ Doctoral Training Partnership studentship from the Natural Environment Research Council (NERC, grant number NE/L002434/1). TMG, CJW and NJM are supported by NERC (NE/R001391/1 and NE/R001235/1) and CJW by a Royal Society University Research Fellowship (URF\R\221023)

## CRedit authorship contribution statement

Conceptualisation: CJW and NJM; Data curation: SMD, NPH, TM-G, P-DP and MJT; Formal analysis: SMD and NPH; Investigation: SMD and NPH; Methodology: SMD, NPH, CJW and NJM; Project administration: CJW; Resources: CJW, NJM and TM-G; Software: SMD and NPH; Supervision: CJW, NJM and TM-G; Validation: NPH, CJW, NJM and TM-G; Visualization: SMD and CJW; Writing – original draft: SMD; Writing - review and editing: SMD, NPH, CJW and TM-G.

534

**References**

535

536

537

538

539

540

541

542

543

544

545

546

547

548

549

550

551

552

553

554

555

556

557

558

559

560

561

562

563

564

565

566

567

568

569

570

571

572

573

574

575

576

577

578

579

580

581

582

583

584

585

586

587

588

- Alexander, M. J., Geller, M., McLandress, C., Polavarapu, S., Preusse, P., Sassi, F., ... Watanabe, S. (2010, July). Recent developments in gravity-wave effects in climate models and the global distribution of gravity-wave momentum flux from observations and models. *Quarterly Journal of the Royal Meteorological Society*, *136*(650), 1103–1124. Retrieved from <https://doi.org/10.1002/qj.637> doi: 10.1002/qj.637
- Alexander, M. J., & Teitelbaum, H. (2007, November). Observation and analysis of a large amplitude mountain wave event over the antarctic peninsula. *Journal of Geophysical Research*, *112*(D21). Retrieved from <https://doi.org/10.1029/2006jd008368> doi: 10.1029/2006jd008368
- Baker, D. J., & Stair, A. T. (1988, April). Rocket measurements of the altitude distributions of the hydroxyl airglow. *Physica Scripta*, *37*(4), 611–622. Retrieved from <https://doi.org/10.1088/0031-8949/37/4/021> doi: 10.1088/0031-8949/37/4/021
- Baumgaertner, A. J. G., & McDonald, A. J. (2007, March). A gravity wave climatology for antarctica compiled from challenging minisatellite payload/global positioning system (CHAMP/GPS) radio occultations. *Journal of Geophysical Research*, *112*(D5). Retrieved from <https://doi.org/10.1029/2006jd007504> doi: 10.1029/2006jd007504
- Becker, E. (2012, October). Dynamical control of the middle atmosphere. *Space Science Reviews*, *168*(1-4), 283–314. Retrieved from <https://doi.org/10.1007/s11214-011-9841-5> doi: 10.1007/s11214-011-9841-5
- Beldon, C., Muller, H., & Mitchell, N. (2006, March). The 8-hour tide in the mesosphere and lower thermosphere over the UK, 1988–2004. *Journal of Atmospheric and Solar-Terrestrial Physics*, *68*(6), 655–668. Retrieved from <https://doi.org/10.1016/j.jastp.2005.10.004> doi: 10.1016/j.jastp.2005.10.004
- Cao, B., & Liu, A. Z. (2016, January). Intermittency of gravity wave momentum flux in the mesopause region observed with an all-sky airglow imager. *Journal of Geophysical Research: Atmospheres*, *121*(2), 650–663. Retrieved from <https://doi.org/10.1002/2015jd023802> doi: 10.1002/2015jd023802
- Cao, B., & Liu, A. Z. (2022, June). Statistical characteristics of high-frequency gravity waves observed by an airglow imager at andes lidar observatory. *Earth and Space Science*, *9*(6). Retrieved from <https://doi.org/10.1029/2022ea002256> doi: 10.1029/2022ea002256
- Davis, R. N., Du, J., Smith, A. K., Ward, W. E., & Mitchell, N. J. (2013, September). The diurnal and semidiurnal tides over ascension island (° s, 14° w) and their interaction with the stratospheric quasi-biennial oscillation: studies with meteor radar, eCMAM and WACCM. *Atmospheric Chemistry and Physics*, *13*(18), 9543–9564. Retrieved from <https://doi.org/10.5194/acp-13-9543-2013> doi: 10.5194/acp-13-9543-2013
- Dempsey, S. M., Hindley, N. P., Moffat-Griffin, T., Wright, C. J., Smith, A. K., Du, J., & Mitchell, N. J. (2021, January). Winds and tides of the antarctic mesosphere and lower thermosphere: One year of meteor-radar observations over rothera (68°s, 68°w) and comparisons with WACCM and eCMAM. *Journal of Atmospheric and Solar-Terrestrial Physics*, *212*, 105510. Retrieved from <https://doi.org/10.1016/j.jastp.2020.105510> doi: 10.1016/j.jastp.2020.105510
- Ejiri, M. K., Shiokawa, K., Ogawa, T., Igarashi, K., Nakamura, T., & Tsuda, T. (2003, November). Statistical study of short-period gravity waves in OH and OI nightglow images at two separated sites. *Journal of Geophysical Research: Atmospheres*, *108*(D21). Retrieved from <https://doi.org/10.1029/2002jd002795> doi: 10.1029/2002jd002795
- Fritts, D. C., & Alexander, M. J. (2003, March). Gravity wave dynamics and ef-

- 589       fects in the middle atmosphere. *Reviews of Geophysics*, 41(1). Retrieved from  
590       <https://doi.org/10.1029/2001rg000106> doi: 10.1029/2001rg000106
- 591       Fritts, D. C., Vadas, S. L., Wan, K., & Werne, J. A. (2006, February). Mean  
592       and variable forcing of the middle atmosphere by gravity waves. *Journal of Atmospheric and Solar-Terrestrial Physics*, 68(3-5), 247–265. Re-  
593       trieved from <https://doi.org/10.1016/j.jastp.2005.04.010> doi:  
594       10.1016/j.jastp.2005.04.010
- 595       Ganaie, B. A., Ramkumar, T., Bhat, A. H., & Malik, M. A. (2022, July). Im-  
596       ager observation of concentric mesospheric gravity waves over srinagar,  
597       jammu and kashmir, india. *Advances in Space Research*, 70(2), 427–439.  
598       Retrieved from <https://doi.org/10.1016/j.asr.2022.04.035> doi:  
599       10.1016/j.asr.2022.04.035
- 600       Gardner, C. S., & Taylor, M. J. (1998). Observational limits for lidar, radar,  
601       and airglow imager measurements of gravity wave parameters. *Journal of*  
602       *Geophysical Research: Atmospheres*, 103(D6), 6427–6437. Retrieved from  
603       <https://agupubs.onlinelibrary.wiley.com/doi/abs/10.1029/97JD03378>  
604       doi: <https://doi.org/10.1029/97JD03378>
- 605       Geller, M. A., Alexander, M. J., Love, P. T., Bacmeister, J., Ern, M., Hertzog, A.,  
606       ... Zhou, T. (2013, August). A comparison between gravity wave momentum  
607       fluxes in observations and climate models. *Journal of Climate*, 26(17), 6383–  
608       6405. Retrieved from <https://doi.org/10.1175/jcli-d-12-00545.1> doi:  
609       10.1175/jcli-d-12-00545.1
- 610       Goldberg, R. A. (2004). The MaCWAVE/MIDAS rocket and ground-based measure-  
611       ments of polar summer dynamics: Overview and mean state structure. *Geo-*  
612       *physical Research Letters*, 31(24). Retrieved from <https://doi.org/10.1029/2004gl019411> doi: 10.1029/2004gl019411
- 613       Hecht, J. H. (2002). An observation of a fast external atmospheric acoustic-gravity  
614       wave. *Journal of Geophysical Research*, 107(D20). Retrieved from [https://](https://doi.org/10.1029/2001jd001438)  
615       [doi.org/10.1029/2001jd001438](https://doi.org/10.1029/2001jd001438) doi: 10.1029/2001jd001438
- 616       Hecht, J. H., Walterscheid, R. L., Hickey, M. P., & Franke, S. J. (2001, March).  
617       Climatology and modeling of quasi-monochromatic atmospheric gravity  
618       waves observed over urbana illinois. *Journal of Geophysical Research: At-*  
619       *mospheres*, 106(D6), 5181–5195. Retrieved from <https://doi.org/10.1029/2000jd900722> doi: 10.1029/2000jd900722
- 620       Hindley, N. P., Cobbett, N., Fritts, D. C., Janchez, D., Mitchell, N. J., Moffat-  
621       Griffin, T., ... Wright, C. J. (2022, December). Radar observations of winds,  
622       waves and tides in the mesosphere and lower thermosphere over south georgia  
623       island (54°s, 36°w) and comparison to WACCM simulations. *ACP*. Retrieved  
624       from <https://doi.org/10.5194/acp-2021-981> doi: 10.5194/acp-2021-981
- 625       Hindley, N. P., Smith, N. D., Wright, C. J., Rees, D. A. S., & Mitchell, N. J. (2016,  
626       June). A two-dimensional stockwell transform for gravity wave analysis of  
627       AIRS measurements. *Atmospheric Measurement Techniques*, 9(6), 2545–  
628       2565. Retrieved from <https://doi.org/10.5194/amt-9-2545-2016> doi:  
629       10.5194/amt-9-2545-2016
- 630       Hindley, N. P., Wright, C. J., Smith, N. D., Hoffmann, L., Holt, L. A., Alexander,  
631       M. J., ... Mitchell, N. J. (2019, December). Gravity waves in the winter  
632       stratosphere over the southern ocean: high-resolution satellite observations and  
633       3-d spectral analysis. *Atmospheric Chemistry and Physics*, 19(24), 15377–  
634       15414. Retrieved from <https://doi.org/10.5194/acp-19-15377-2019> doi:  
635       10.5194/acp-19-15377-2019
- 636       Hindley, N. P., Wright, C. J., Smith, N. D., & Mitchell, N. J. (2015, July). The  
637       southern stratospheric gravity wave hot spot: individual waves and their mo-  
638       mentum fluxes measured by COSMIC GPS-RO. *Atmospheric Chemistry and*  
639       *Physics*, 15(14), 7797–7818. Retrieved from [https://doi.org/10.5194/](https://doi.org/10.5194/acp-15-7797-2015)  
640       [acp-15-7797-2015](https://doi.org/10.5194/acp-15-7797-2015) doi: 10.5194/acp-15-7797-2015

- 644 Hocking, W., Fuller, B., & Vandeppeer, B. (2001, January). Real-time determi-  
 645 nation of meteor-related parameters utilizing modern digital technology.  
 646 *Journal of Atmospheric and Solar-Terrestrial Physics*, *63*(2-3), 155–169.  
 647 Retrieved from [https://doi.org/10.1016/s1364-6826\(00\)00138-3](https://doi.org/10.1016/s1364-6826(00)00138-3) doi:  
 648 10.1016/s1364-6826(00)00138-3
- 649 Hu, S., Ma, S., Yan, W., Hindley, N. P., Xu, K., & Jiang, J. (2019a, January).  
 650 Measuring gravity wave parameters from a nighttime satellite low-light im-  
 651 age based on two-dimensional stockwell transform. *Journal of Atmospheric*  
 652 *and Oceanic Technology*, *36*(1), 41–51. Retrieved from [https://doi.org/](https://doi.org/10.1175/jtech-d-18-0092.1)  
 653 [10.1175/jtech-d-18-0092.1](https://doi.org/10.1175/jtech-d-18-0092.1) doi: 10.1175/jtech-d-18-0092.1
- 654 Hu, S., Ma, S., Yan, W., Hindley, N. P., Xu, K., & Jiang, J. (2019b, January).  
 655 Measuring gravity wave parameters from a nighttime satellite low-light im-  
 656 age based on two-dimensional stockwell transform. *Journal of Atmospheric*  
 657 *and Oceanic Technology*, *36*(1), 41–51. Retrieved from [https://doi.org/](https://doi.org/10.1175/jtech-d-18-0092.1)  
 658 [10.1175/jtech-d-18-0092.1](https://doi.org/10.1175/jtech-d-18-0092.1) doi: 10.1175/jtech-d-18-0092.1
- 659 Hu, S., Ma, S., Yan, W., Hindley, N. P., & Zhao, X. (2019, April). Measuring inter-  
 660 nal solitary wave parameters based on VIIRS/DNB data. *International Jour-*  
 661 *nal of Remote Sensing*, *40*(20), 7805–7816. Retrieved from [https://doi.org/](https://doi.org/10.1080/01431161.2019.1608389)  
 662 [10.1080/01431161.2019.1608389](https://doi.org/10.1080/01431161.2019.1608389) doi: 10.1080/01431161.2019.1608389
- 663 Kalisch, S., Preusse, P., Ern, M., Eckermann, S. D., & Riese, M. (2014). Differences  
 664 in gravity wave drag between realistic oblique and assumed vertical propaga-  
 665 tion. *Journal of Geophysical Research: Atmospheres*, *119*(17), 10,081–10,099.  
 666 Retrieved from [https://agupubs.onlinelibrary.wiley.com/doi/abs/](https://agupubs.onlinelibrary.wiley.com/doi/abs/10.1002/2014JD021779)  
 667 [10.1002/2014JD021779](https://doi.org/10.1002/2014JD021779) doi: <https://doi.org/10.1002/2014JD021779>
- 668 Kam, H., Jee, G., Kim, Y., bae Ham, Y., & Song, I-S. (2017, March). Statisti-  
 669 cal analysis of mesospheric gravity waves over king sejong station, antarctica  
 670 (62.2°s, 58.8°w). *Journal of Atmospheric and Solar-Terrestrial Physics*, *155*,  
 671 86–94. Retrieved from <https://doi.org/10.1016/j.jastp.2017.02.006>  
 672 doi: 10.1016/j.jastp.2017.02.006
- 673 Khomich, V. Y., Semenov, A. I., & Shefov, N. N. (2008). *Airglow as an indicator*  
 674 *of upper atmospheric structure and dynamics*. Springer Science & Business Me-  
 675 dia.
- 676 Kogure, M., Yue, J., & Liu, H. (2021, April). Gravity wave weakening during  
 677 the 2019 antarctic stratospheric sudden warming. *Geophysical Research Let-*  
 678 *ters*, *48*(8). Retrieved from <https://doi.org/10.1029/2021gl092537> doi:  
 679 10.1029/2021gl092537
- 680 Kogure, M., Yue, J., Nakamura, T., Hoffmann, L., Vadas, S. L., Tomikawa, Y.,  
 681 ... Janches, D. (2020, September). First direct observational evidence for  
 682 secondary gravity waves generated by mountain waves over the andes. *Geo-*  
 683 *physical Research Letters*, *47*(17). Retrieved from [https://doi.org/10.1029/](https://doi.org/10.1029/2020gl088845)  
 684 [2020gl088845](https://doi.org/10.1029/2020gl088845) doi: 10.1029/2020gl088845
- 685 Li, J., Li, T., Dou, X., Fang, X., Cao, B., She, C.-Y., ... Thorsen, D. (2017, March).  
 686 Characteristics of ripple structures revealed in OH airglow images. *Journal*  
 687 *of Geophysical Research: Space Physics*, *122*(3), 3748–3759. Retrieved from  
 688 <https://doi.org/10.1002/2016ja023538> doi: 10.1002/2016ja023538
- 689 Li, Z., Liu, A., & Sivjee, G. G. (2014, April). Removing milky way from airglow  
 690 images using principal component analysis. *Journal of Atmospheric and*  
 691 *Solar-Terrestrial Physics*, *110-111*, 50–57. Retrieved from [https://doi.org/](https://doi.org/10.1016/j.jastp.2014.01.016)  
 692 [10.1016/j.jastp.2014.01.016](https://doi.org/10.1016/j.jastp.2014.01.016) doi: 10.1016/j.jastp.2014.01.016
- 693 Li, Z., Liu, A. Z., Lu, X., Swenson, G. R., & Franke, S. J. (2011, November).  
 694 Gravity wave characteristics from OH airglow imager over maui. *Journal*  
 695 *of Geophysical Research: Atmospheres*, *116*(D22), n/a–n/a. Retrieved from  
 696 <https://doi.org/10.1029/2011jd015870> doi: 10.1029/2011jd015870
- 697 Lindzen, R. S. (1981). Turbulence and stress owing to gravity wave and tidal  
 698 breakdown. *Journal of Geophysical Research*, *86*(C10), 9707. Retrieved from

- 699 <https://doi.org/10.1029/jc086ic10p09707> doi: 10.1029/jc086ic10p09707  
700 Matsuda, T. S., Nakamura, T., Ejiri, M. K., Tsutsumi, M., & Shiokawa, K. (2014,  
701 August). New statistical analysis of the horizontal phase velocity distri-  
702 bution of gravity waves observed by airglow imaging. *Journal of Geo-*  
703 *physical Research: Atmospheres*, *119*(16), 9707–9718. Retrieved from  
704 <https://doi.org/10.1002/2014jd021543> doi: 10.1002/2014jd021543
- 705 McDonald, A. J. (2012, August). Gravity wave occurrence statistics derived from  
706 paired COSMIC/FORMOSAT3 observations. *Journal of Geophysical Research:*  
707 *Atmospheres*, *117*(D15), n/a–n/a. Retrieved from [https://doi.org/10.1029/](https://doi.org/10.1029/2011jd016715)  
708 [2011jd016715](https://doi.org/10.1029/2011jd016715) doi: 10.1029/2011jd016715
- 709 Meinel, I. A. B. (1950, May). OH emission bands in the spectrum of the night  
710 sky. *The Astrophysical Journal*, *111*, 555. Retrieved from [https://doi.org/](https://doi.org/10.1086/145296)  
711 [10.1086/145296](https://doi.org/10.1086/145296) doi: 10.1086/145296
- 712 Miller, S. D., Straka, W. C., Yue, J., Smith, S. M., Alexander, M. J., Hoffmann,  
713 L., ... Partain, P. T. (2015, November). Upper atmospheric gravity wave  
714 details revealed in nightglow satellite imagery. *Proceedings of the National*  
715 *Academy of Sciences*, *112*(49). Retrieved from [https://doi.org/10.1073/](https://doi.org/10.1073/pnas.1508084112)  
716 [pnas.1508084112](https://doi.org/10.1073/pnas.1508084112) doi: 10.1073/pnas.1508084112
- 717 Mitchell, N. J. (2002). Mean winds and tides in the arctic mesosphere and lower  
718 thermosphere. *Journal of Geophysical Research*, *107*(A1). Retrieved from  
719 <https://doi.org/10.1029/2001ja900127> doi: 10.1029/2001ja900127
- 720 Moffat-Griffin, T., & Colwell, S. R. (2017, September). The characteristics of  
721 the lower stratospheric gravity wavefield above halley (75°s, 26°w), antar-  
722 tica, from radiosonde observations. *Journal of Geophysical Research: Atmo-*  
723 *spheres*, *122*(17), 8998–9010. Retrieved from [https://doi.org/10.1002/](https://doi.org/10.1002/2017jd027079)  
724 [2017jd027079](https://doi.org/10.1002/2017jd027079) doi: 10.1002/2017jd027079
- 725 Nielsen, K. (2007). *Climatology and case studies of mesospheric gravity waves ob-*  
726 *erved at polar latitudes*. Utah State University.
- 727 Nielsen, K., Taylor, M., Hibbins, R., & Jarvis, M. (2009, June). Climatology of  
728 short-period mesospheric gravity waves over halley, antarctica (76°s, 27°w).  
729 *Journal of Atmospheric and Solar-Terrestrial Physics*, *71*(8-9), 991–1000.  
730 Retrieved from <https://doi.org/10.1016/j.jastp.2009.04.005> doi:  
731 [10.1016/j.jastp.2009.04.005](https://doi.org/10.1016/j.jastp.2009.04.005)
- 732 Nielsen, K., Taylor, M. J., Pautet, P.-D., Fritts, D. C., Mitchell, N., Beldon, C.,  
733 ... Goldberg, R. A. (2006, July). Propagation of short-period gravity waves  
734 at high-latitudes during the MaCWAVE winter campaign. *Annales Geo-*  
735 *physicae*, *24*(4), 1227–1243. Retrieved from [https://doi.org/10.5194/](https://doi.org/10.5194/angeo-24-1227-2006)  
736 [angeo-24-1227-2006](https://doi.org/10.5194/angeo-24-1227-2006) doi: 10.5194/angeo-24-1227-2006
- 737 Pautet, P.-D. (2005). Climatology of short-period gravity waves observed over  
738 northern australia during the darwin area wave experiment (DAWEX)  
739 and their dominant source regions. *Journal of Geophysical Research*,  
740 *110*(D3). Retrieved from <https://doi.org/10.1029/2004jd004954> doi:  
741 [10.1029/2004jd004954](https://doi.org/10.1029/2004jd004954)
- 742 Perrett, J. A., Wright, C. J., Hindley, N. P., Hoffmann, L., Mitchell, N. J., Preusse,  
743 P., ... Eckermann, S. D. (2021, January). Determining gravity wave  
744 sources and propagation in the southern hemisphere by ray-tracing AIRS  
745 measurements. *Geophysical Research Letters*, *48*(2). Retrieved from  
746 <https://doi.org/10.1029/2020gl088621> doi: 10.1029/2020gl088621
- 747 Peterson, A. W. (1979, Oct). Airglow events visible to the naked eye. *Appl.*  
748 *Opt.*, *18*(20), 3390–3393. Retrieved from [http://opg.optica.org/ao/](http://opg.optica.org/ao/abstract.cfm?URI=ao-18-20-3390)  
749 [abstract.cfm?URI=ao-18-20-3390](http://opg.optica.org/ao/abstract.cfm?URI=ao-18-20-3390) doi: 10.1364/AO.18.003390
- 750 Rourke, S., Mulligan, F. J., French, W. J. R., & Murphy, D. J. (2017). A clima-  
751 tological study of short-period gravity waves and ripples at davis station,  
752 antarctica (68°s, 78°e), during the (austral winter february–october) period  
753 1999–2013. *Journal of Geophysical Research: Atmospheres*, *122*(21), 11,388–

- 754 11,404. Retrieved from <https://agupubs.onlinelibrary.wiley.com/doi/abs/10.1002/2017JD026998> doi: <https://doi.org/10.1002/2017JD026998>
- 755
- 756 Sedlak, R., Zuhr, A., Schmidt, C., Wüst, S., Bittner, M., Didebulidze, G. G., &  
757 Price, C. (2020, September). Intra-annual variations of spectrally re-  
758 solved gravity wave activity in the upper mesosphere/lower thermosphere  
759 (UMLT) region. *Atmospheric Measurement Techniques*, *13*(9), 5117–  
760 5128. Retrieved from <https://doi.org/10.5194/amt-13-5117-2020> doi:  
761 10.5194/amt-13-5117-2020
- 762 Stober, G., Kuchar, A., Pokhotelov, D., Liu, H., Liu, H.-L., Schmidt, H., ...  
763 Mitchell, N. (2021, September). Interhemispheric differences of meso-  
764 sphere–lower thermosphere winds and tides investigated from three whole-  
765 atmosphere models and meteor radar observations. *Atmospheric Chem-  
766 istry and Physics*, *21*(18), 13855–13902. Retrieved from <https://doi.org/10.5194/acp-21-13855-2021> doi:  
767 10.5194/acp-21-13855-2021
- 768 Stockwell, R., Mansinha, L., & Lowe, R. (1996). Localization of the complex spec-  
769 trum: the s transform. *IEEE Transactions on Signal Processing*, *44*(4), 998–  
770 1001. doi: 10.1109/78.492555
- 771 Stockwell, R. G., & Lowe, R. P. (2001, August). Airglow imaging of gravity waves:  
772 1. results from a small network of OH nightglow scanning imagers. *Journal of  
773 Geophysical Research: Atmospheres*, *106*(D15), 17185–17203. Retrieved from  
774 <https://doi.org/10.1029/2001jd900035> doi: 10.1029/2001jd900035
- 775 Takahashi, H., Melo, S. M. L., Clemesha, B. R., Simonich, D. M., Stegman, J., &  
776 Witt, G. (1996, February). Atomic hydrogen and ozone concentrations derived  
777 from simultaneous lidar and rocket airglow measurements in the equatorial re-  
778 gion. *Journal of Geophysical Research: Atmospheres*, *101*(D2), 4033–4040. Re-  
779 trieved from <https://doi.org/10.1029/95jd03035> doi: 10.1029/95jd03035
- 780 Taylor, M. J., Pendleton, W. R., Clark, S., Takahashi, H., Gobbi, D., & Goldberg,  
781 R. A. (1997, November). Image measurements of short-period gravity waves at  
782 equatorial latitudes. *Journal of Geophysical Research: Atmospheres*, *102*(D22),  
783 26283–26299. Retrieved from <https://doi.org/10.1029/96jd03515> doi:  
784 10.1029/96jd03515
- 785 Taylor, M. J., Ryan, E. H., Tuan, T. F., & Edwards, R. (1993, April). Evidence  
786 of preferential directions for gravity wave propagation due to wind filtering  
787 in the middle atmosphere. *Journal of Geophysical Research: Space Physics*,  
788 *98*(A4), 6047–6057. Retrieved from <https://doi.org/10.1029/92ja02604>  
789 doi: 10.1029/92ja02604
- 790 von Savigny, C. (2015, May). Variability of OH(3–1) emission altitude from 2003  
791 to 2011: Long-term stability and universality of the emission rate–altitude  
792 relationship. *Journal of Atmospheric and Solar-Terrestrial Physics*, *127*, 120–  
793 128. Retrieved from <https://doi.org/10.1016/j.jastp.2015.02.001> doi:  
794 10.1016/j.jastp.2015.02.001
- 795 Wright, C. J., & Gille, J. C. (2013, May). Detecting overlapping gravity waves us-  
796 ing the s-transform. *Geophysical Research Letters*, *40*(9), 1850–1855. Retrieved  
797 from <https://doi.org/10.1002/grl.50378> doi: 10.1002/grl.50378
- 798 Wright, C. J., Hindley, N. P., Hoffmann, L., Alexander, M. J., & Mitchell, N. J.  
799 (2017, July). Exploring gravity wave characteristics in 3-d using a novel  
800 s-transform technique: AIRS/aqua measurements over the southern andes  
801 and drake passage. *Atmospheric Chemistry and Physics*, *17*(13), 8553–  
802 8575. Retrieved from <https://doi.org/10.5194/acp-17-8553-2017> doi:  
803 10.5194/acp-17-8553-2017
- 804 Wüst, S., & Bittner, M. (2008, March). Gravity wave reflection: Case study based  
805 on rocket data. *Journal of Atmospheric and Solar-Terrestrial Physics*, *70*(5),  
806 742–755. Retrieved from <https://doi.org/10.1016/j.jastp.2007.10.010>  
807 doi: 10.1016/j.jastp.2007.10.010
- 808 Wüst, S., Bittner, M., Espy, P. J., French, W. J. R., & Mulligan, F. J. (2022, Au-

- 809           gust). Hydroxyl airglow observations for investigating atmospheric dynamics:  
810           results and challenges. *Atmospheric Chemistry and Physics*. Retrieved from  
811           <https://doi.org/10.5194/acp-2022-528> doi: 10.5194/acp-2022-528
- 812       Wüst, S., Bittner, M., Yee, J.-H., Mlynčzak, M. G., & III, J. M. R. (2017, Decem-  
813       ber). Variability of the brunt-väisälä frequency at the OH\* layer height. *Atmo-  
814       spheric Measurement Techniques*, *10*(12), 4895–4903. Retrieved from [https://  
815       doi.org/10.5194/amt-10-4895-2017](https://doi.org/10.5194/amt-10-4895-2017) doi: 10.5194/amt-10-4895-2017
- 816       Wüst, S., Wendt, V., Schmidt, C., Lichtenstern, S., Bittner, M., Yee, J.-H., ...  
817       III, J. M. R. (2016, February). Derivation of gravity wave potential energy  
818       density from NDMC measurements. *Journal of Atmospheric and Solar-  
819       Terrestrial Physics*, *138-139*, 32–46. Retrieved from [https://doi.org/  
820       10.1016/j.jastp.2015.12.003](https://doi.org/10.1016/j.jastp.2015.12.003) doi: 10.1016/j.jastp.2015.12.003
- 821       Yoshimura, R., Iwagami, N., & Oyama, K.-I. (2003, September). Rocket mea-  
822       surement of electron density and atomic oxygen density modulated by at-  
823       mospheric gravity waves. *Advances in Space Research*, *32*(5), 837–842. Re-  
824       trieved from [https://doi.org/10.1016/s0273-1177\(03\)00422-8](https://doi.org/10.1016/s0273-1177(03)00422-8) doi:  
825       10.1016/s0273-1177(03)00422-8